Astrophysics and Space Science (2022) 367:50
https://doi.org/10.1007/s10509-022-04074-1

ORIGINAL ARTICLE

Age-velocity relations with *GALEX* FUV-determined ages of Sun-like, solar neighborhood stars

Sara Crandall[1] · Graeme H. Smith[2] · Sufia Birmingham[3] · Vy Vo[4] · Constance Rockosi[1] · Ruth Murray-Clay[1]

Received: 3 October 2021 / Accepted: 24 April 2022 / Published online: 23 May 2022

Abstract
A relationship between chromospheric activity and age is calibrated for FGK dwarf stars using *GALEX* FUV magnitudes and *Gaia* ($G_{BP} - G$) colors. Such a calibration between *GALEX* FUV magnitudes and stellar age has utility in population studies of dwarfs for further understanding of the chemical evolution of the Milky Way. As an illustration of one such application we have investigated a population of Sun-like, solar neighborhood stars for their metallicities and velocity dispersions; a cross-matched sample of FGK type dwarf stars from Casagrande et al. (2011) with the *Gaia* and *GALEX* catalogs. Using calibrated relationships between FUV magnitudes and age, we determined a chromospheric activity indicator, Q, and stellar age, τ, for each dwarf. We constructed age-velocity (AVR) and age-metallicity (AMR) relations with empirically-determined FUV ages. Power law fits to AVR plots are consistent with heating mechanism models within the literature. We further demonstrate that perigalactic distance and eccentricity versus FUV-age plots are consistent with an "inside out" formation history model.

Keywords Planet hosting stars · Milky Way disk · Galactic archaeology

1 Introduction

The velocity dispersion of solar neighborhood, FGK main sequence stars has been shown to increase with age. This so-called age-velocity dispersion relation (AVR) has a long history of examination (Strömberg 1946; Spitzer and Schwarzschild 1951; Wielen 1977; Seabroke and Gilmore 2007; Soubiran et al. 2008). Constraints on this relation lend to a better understanding of the mechanisms which define the formation and evolution of the Milky Way galaxy. The velocity dispersion increase with stellar age may be the result of several factors, including how the Milky Way initially formed. Rix and Bovy (2013) reviews the study of Galactic evolution and mechanisms that may have played a role to form the current state of the AVR. One explanation posits that orbits of stars were determined at birth. Vertical gradients of age and metallicity in this case are established as a consequence of the gas settlement of the disk, and radial gradients are formed "inside out" (see e.g. Veltx et al. 2008; Robin et al. 2014; Navarro et al. 2018). The initial determination of orbits and trends in star formation (Bird et al. 2013) may have been the result of several mechanisms, including early mergers (Brook et al. 2004, 2012) and accretion from satellite galaxies (Abadi et al. 2003). Alternately, the observed AVR is often argued to be the result of orbital scattering or dynamical heating of a stellar distribution after gas settled into a thin disk. As such, older stars subsequently had more time to gravitationally interact with other massive objects and become scattered into altered orbits.

A number of numerical modelling studies have been made to explore the latter possibility that heating mechanisms may play a significant role in producing the observed AVR. Simulations have demonstrated how gravitational interactions can cause heating through a variety of mechanisms. In earlier studies Giant Molecular Clouds (GMCs) were presumed to be the main driver of Galactic heating (Spitzer and Schwarzschild 1951, 1953), yet in recent years simulations have shown that multiple mechanisms contribute to the observed AVR (see, for example, Hänninen and Flynn 2002; Aumer et al. 2016). The spiral arm structure and a possible bar (Barbanis and Woltjer 1967; Aumer

✉ S. Crandall
sacranda@ucsc.edu

[1] Department of Astronomy and Astrophysics, University of California, Santa Cruz, CA, 95064, USA

[2] University of California Observatories/Lick Observatory, University of California, Santa Cruz, CA 95064, USA

[3] Turlock High School, Turlock, USA

[4] East Side Union High School, San Jose, USA

et al. 2016), black holes (Lacey and Ostriker 1985; Hänninen and Flynn 2002), and satellite mergers (Walker et al. 1996; Moetazedian and Just 2016; Ting and Rix 2019) may all play a role in Galactic heating. The resulting models can be tested with observations of the Solar neighborhood AVR. In this work we qualitatively investigate possible heating mechanisms that played a role in the initial galaxy formation and those involved in the evolution of the AVR.

More often than not, the stellar ages utilized in observational determinations of the local AVR are based upon isochrone-determination techniques. In isochrone fitting one makes use of a comparison between an observed color magnitude diagram which contains the stars of interest and theoretical isochrones or evolutionary tracks for stellar models of varied ages. This method is useful when age-dating coevolved stars such as clusters and moving groups, but can result in uncertain ages when age-dating single stars. The Geneva-Copenhagen Survey (GCS) (Nordström et al. 2004) is a large survey well suited for measuring the AVR, and has become the standard for comparison (Holmberg et al. 2009; Casagrande et al. 2011). The GCS contains 16,682 G and F-type stars within the solar neighborhood with metallicity, rotation, age, kinematics, and Galactic orbit determinations. Kinematics for this sample used *Hipparcos* parallaxes, Tycho-2 proper motions, and *uvbyβ* photometry. Stellar ages within the CGS were determined with isochrone modeling. This well-used sample can test our understanding of the Milky Way's evolution by providing the data from which a local stellar AVR can be derived. For example, Fig. 8 of Holmberg et al. (2009), who use distances, ages, and kinematics from the GCS, shows synthetic age-velocity relations for three different disc heating scenarios (scattering, heating saturation, and a late minor merger).

In recent years isochrone ages have been improved through the use of Bayesian techniques. However, in Figure 4a of Lin et al. (2018) stars older than ∼2 Gyr still have significant scatter between their improved Bayesian-determined ages and those found elsewhere within the literature. Such scatter illustrates a need for additional types of age-dating techniques which may be applied to single stars. Then one may compare AVRs constructed with stellar ages determined from a variety of methods. Ages of FGK main sequence stars based on the time-varying behavior of stellar activity can provide one such potential alternative (Strömberg 1946; Roman 1950a,b).

In Crandall et al. (2020) the stellar activity-age relationship is the basis of a calibration between stellar age and far-ultraviolet (FUV) brightness which can be added to the toolbox of other age-dating techniques. Therein FUV magnitude observations from the Galaxy Evolution Explorer telescope (*GALEX*) are shown to be tracers of chromospheric activity (see e.g. Smith and Redenbaugh 2010) and hence age (Findeisen et al. 2011). Crandall et al. (2020) derived an FUV-age calibration through which ages may be determined without introducing errors associated with model-based methodologies, such as isochrone fitting.

The FUV-age relationship in Crandall et al. (2020) is calibrated in a combined *GALEX* FUV and Johnson B and V color space. In Sect. 2 of this work we re-calibrate the relationship in a *GALEX* plus *Gaia* color space, as *Gaia* photometry is now available for a much larger number of stars than is $(B-V)$ photometry. In Sect. 3 the updated FUV-age calibration is utilized to determine model-independent ages of 660 GCS stars. A stellar AVR is constructed using FUV-determined ages and unprecedentedly precise *Gaia* kinematics. The resultant observational AVR is fitted to a power law whose coefficients are compared with other determinations in the literature. Finally, we utilize perigalactic radii, eccentricities, and FUV-determined ages to show that the stars in our sample follow an "inside out" and "upside down" formation history pattern. Section 5 summarizes our findings.

2 A far-ultraviolet excess correlation with stellar age

Far-ultraviolet (FUV) emission has been shown to be an indicator of chromospheric activity and hence age (Smith and Redenbaugh 2010; Findeisen et al. 2011; Smith et al. 2017) among FGK main sequence stars. Within Crandall et al. (2020), this relationship was characterized such that one may use *GALEX* FUV magnitudes and Johnson $(B-V)$ colors to estimate the age of FGK dwarf stars. The relationship takes the form

$$\log_e(\tau) = \log_e(a) + bQ, \tag{1}$$

where τ is the stellar age in Gyr, Q is an FUV-excess parameter, and a and b are linear fit parameters. The Q parameter is dependent on *GALEX* FUV magnitude and Johnson $(B-V)$ color. The fit parameters a and b are also dependent on $(B-V)$. However, $(B-V)$ colors are not always available for a stellar sample. With the recent *Gaia* data releases we find that *Gaia* colors are now available for many more Galactic FGK stars than Johnson photometry. As such, within this section we establish a new FUV-age relationship for Sun-like stars through the use of *Gaia* colors.

2.1 Data compilation

Development of our new age-calibration comes from an FUV-based analysis similar to that of Crandall et al. (2020) in which stellar age data from four catalogs were combined to produce a set of calibration stars. Each of these catalogs, Ballering et al. (2013), Isaacson and Fischer (2010), Sierchio et al. (2014), Lorenzo-Oliveira et al. (2018), contain

FGK dwarf stars with solar-like luminosities, metallicities, and spectral types. The ages in these four catalogs were primarily determined by stellar activity indicators such as the chromospheric Ca II H plus K emission line index $\log R'_{\rm HK}$. Ballering et al. (2013) and Sierchio et al. (2014) utilized chromospheric and X-ray activity indicators supplemented with surface gravity measurements and gyrochronology, where available, to derive stellar ages. Their resulting age values were then checked against isochrone-determined estimates for consistency. Ages computed in Isaacson and Fischer (2010) were derived via $\log R'_{\rm HK}$ and calibrations from Mamajek and Hillenbrand (2008). Finally, ages for a few stars in our sample from Lorenzo-Oliveira et al. (2018) were solely estimated from Yonsei-Yale isochrones (Yi et al. 2001; Kim et al. 2002).[1] The oldest star in our sample is 9 Gyr.

Many of the stars in the catalogs have *GALEX* FUV and *Gaia* G_{BP} and G magnitudes, information vital to the FUV-age calibration. The *GALEX* far-ultraviolet magnitudes were extracted from the GR6/7 data release by use of the Mikulski Archive for Space Telescopes (Conti et al. 2011). Many of the said FUV magnitudes come from images obtained as part of the *GALEX* All-Sky Imaging Survey. Optical *Gaia* magnitudes were collected from Data Release 2 (DR2) and early Data Release 3 (eDR3) (Gaia Collaboration et al. 2018).

Additionally, our sample consisted of stars which have Johnson $(B-V)$ colors for the purpose of extracting stars with Solar-like magnitudes and colors. The Johnson colors were collected from the *Hipparcos* catalog. We only considered those dwarfs which fall into a solar-like color range of $0.55 \leq (B-V) \leq 0.71$ and have an absolute visual magnitude within ± 0.5 mag of the Sun: $4.3 \leq M_{\rm V} \leq 5.3$. The absolute magnitude cut is not removing stars at ages where our FUV calibration will work well (see Sect. 6). More luminous stars that have evolved further from the zero-age main sequence can have weakened chromospheric Ca II H and K emission lines (Wright 2004), which are used for age-dating within the catalogs, and so may have less reliable ages. Absolute magnitudes were determined with *Gaia* parallaxes. These restrictions ensure that the stars considered here have spectral types and luminosities similar to that of the Sun.

After the above color and magnitude cuts were placed on the sample of stars from Isaacson and Fischer (2010), Ballering et al. (2013), Sierchio et al. (2014), Lorenzo-Oliveira et al. (2018), we were left with a collection of 401 stars with Sun-like luminosities, effective temperatures, and spectral types. To address metallicity, a histogram of [Fe/H] is plotted in Fig. 1 for all stars. The metallicity values are taken from Casagrande et al. (2011), and fall within a range of $-1.5 \leq$[Fe/H]≤ 0.76, although the number of calibration stars with [Fe/H] < -0.5 is very small, as can be seen in Fig. 1. Of the stars within the sample, 74% or 295 dwarfs, fall within a solar-like metallicity range of $-0.2 \leq$[Fe/H]≤ 0.2. Most of the sample thus has a Sun-like range in [Fe/H], so that we did not reduce the sample further based on metallicity. There may be a concern with metallicity effects contributing to errors in an FUV-age relationship, however, Figs. 6 and 8 of Crandall et al. (2020) show no correlations between metallicity and this relationship for [Fe/H] > -0.4 dex.

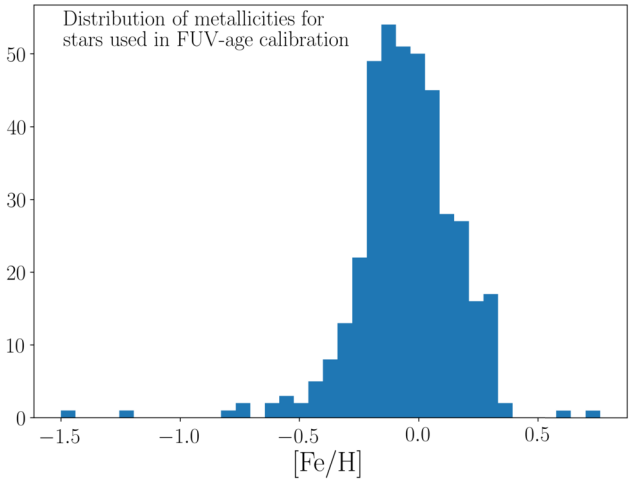

Fig. 1 A metallicity histogram of 401 stars used in the FUV-age calibration. Of the stars within the sample, 74% or 295 dwarfs, fall within a solar-like metallicity range of $-0.2 \leq$[Fe/H]≤ 0.2

2.2 Constraining the FUV-age relation

In a similar manner to Crandall et al. (2020) we define an FUV-excess parameter Q as

$$Q = (FUV - G_{BP}) - u_{\rm FUV}, \tag{2}$$

where G_{BP} is the *Gaia* blue magnitude and $u_{\rm FUV}$ is an upper boundary to the value of $(FUV - G_{BP})$ as a function of $(G_{BP} - G)$. This boundary, which is shown in Fig. 2, represents a minimum chromospheric activity level against which to define an FUV excess, i.e., Q is equal to the difference between the observed $(FUV - G_{BP})$ color and the boundary value at the relevant stellar $(G_{BP} - G)$.

Figure 2 is a two-color diagram of $(FUV - G_{BP})$ versus $(G_{BP} - G)$ for all FGK stars in our calibration sample with optical colors of $0.10 \leq (G_{BP} - G) \leq 0.55$. The few dwarfs outside of this range are very scattered in their two-color relationship and are not included in Fig. 2. A minimum chromospheric boundary, the $u_{\rm FUV}$ function referred to above,

[1] We did not include larger samples of stars with isochrone-determined ages within our calibration sample, because they would have less precise ages. The Lorenzo-Oliveira et al. (2018) sample includes more precise stellar ages due to their use of solar twin stars. They utilized precise spectroscopic parameters and combined them statistically with their luminosities to achieve precise ages. Imprecise luminosities normally used in determining ages with isochrones is not a large contributor to uncertainty in this case.

Table 1 Age Calibration Fits for the FUV-Excess Parameter Q

Bin	$(G_{BP}-G)$ Range	$\langle G_{BP}-G\rangle$[a]	a	b	N[b]	Q_{max}[c]	ρ[d]	r^2[e]	RMS[f]
1	0.27-0.32	0.30	21.97	2.82	238	−0.51	0.82	0.70	0.70
2	0.28-0.33	0.31	19.53	2.61	296	−0.40	0.82	0.75	0.63
3	0.29-0.34	0.32	18.91	2.49	321	−0.40	0.82	0.77	0.63
4	0.30-0.35	0.32	17.70	2.33	293	−0.40	0.80	0.75	0.65
5	0.31-0.36	0.33	18.0	2.24	229	−0.40	0.77	0.82	0.53
6	0.32-0.37	0.33	16.18	2.04	158	−0.40	0.80	0.83	0.53
7	0.33-0.38	0.34	16.89	1.99	89	−0.40	0.78	0.85	0.55
8	0.34-0.39	0.35	15.26	1.68	29	−0.46	0.84	0.90	0.35

[a]Average $(G_{BP}-G)$ color.
[b]Number of stars within each bin.
[c]Q value at which the FUV-age relationship flattens and the fit is truncated.
[d]Spearman coefficient.
[e]Coefficient of determination.
[f]RMS of $\log_e \tau$ about each fit.

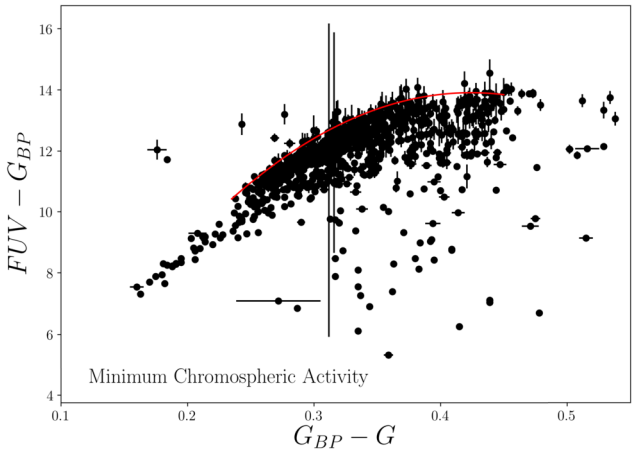

Fig. 2 A FUV-optical two-color diagram of FGK stars from Isaacson and Fischer (2010), Ballering et al. (2013), Sierchio et al. (2014), Lorenzo-Oliveira et al. (2018) with *GALEX* FUV and *Gaia* magnitudes. Within the color range $0.27 \leq (G_{BP}-G) \leq 0.43$ there is a range of $(FUV - G_{BP})$ colors indicating a range of chromospheric activity levels at any given optical color. Red curve depicts an empirical locus of minimum chromospheric activity

is clearly defined in the figure and was fit by the red line therein, which has the equation

$$u_{\rm FUV} = -97.38(G_{BP}-G)^2 + 82.61(G_{BP}-G) - 3.61. \quad (3)$$

Figure 2 also reveals significant spread in values of $(FUV - G_{BP})$ at a given optical color within the range $0.27 < (G_{BP}-G) < 0.43$. Such varied $(FUV - G_{BP})$ behavior demonstrates a range of FUV chromospheric activity levels among FGK dwarfs at a given $(G_{BP}-G)$.

Errors shown in Fig. 2 only reflect *Gaia* magnitude errors. *GALEX* FUV magnitude errors are reported in the GR6/7 data release. However, they are not significant for our uses here. For example, the cross-matched sample described in Sect. 2.1 contains 1,288 stars with FUV magnitude errors. The average magnitude error for this sample is 0.8%, where the percent error was determined by (error in mag)/mag. See Sect. 2.3 for more discussion on errors assumed in our calibration.

To constrain the FUV-age relationship with *Gaia* colors, we plot literature-reported ages from the four samples listed in Sect. 2.1 against the Q values for each star. Following Crandall et al. (2020), the fitting function that we use is a linear equation involving the natural logarithm of the stellar age τ, which is taken to be in units of Gyr throughout this paper. The basic age-calibration equation that we empirically adopt is thus the Equation (1) given above. As shown in Fig. 2 this relationship is dependent on the stellar $(G_{BP}-G)$ color, and so we plot $\log_e \tau$ against Q in color bins. The defined eight *Gaia* color bins are of width 0.5 mag and range between $0.27 \leq (G_{BP}-G) \leq 0.40$, e.g., bin 1 is $0.27 \leq (G_{BP}-G) < 0.32$, bin 2 is $0.28 \leq (G_{BP}-G) < 0.33$, etc. Figure 3 shows the fits in four bins as examples. There is a flattening of the relationship at the most positive Q values, corresponding to the less active stars. The slope changes within each $(G_{BP}-G)$ bin from anywhere between $Q = -0.51$ to $Q = -0.40$. For each bin we then only fit up to the point of flattening, which we call Q_{max}. These values are listed in Table 1.

Duplicate stars from the four samples (Lorenzo-Oliveira et al. 2018; Sierchio et al. 2014; Ballering et al. 2013; Isaacson and Fischer 2010) were treated separately in constraining the FUV-age relationship. That is, no ages were combined in the form of an average or the like. Ages were not combined because the methodologies in deriving ages within the four samples differed significantly enough, with the exception of Ballering et al. (2013) and Sierchio et al. (2014), that we could not reasonably average them.

Table 1 lists the values of fitted age-calibration parameters for each color bin, namely the color range of each bin, average color per bin, number of stars in each bin (N), the maximum FUV-excess Q_{max} to which the fit is made, the linear fit parameters a and b, Spearman's correlation coefficient (ρ), the coefficient of determination (r^2), and the RMS of each fit about $\log_e \tau$. We found reasonably high ρ and r^2 values for each fit indicating that the FUV-age relationship is well fit with the linear function Equation (1).

Extinction can have a significant effect in the UV and optical band. However, we did attempt to test for possible

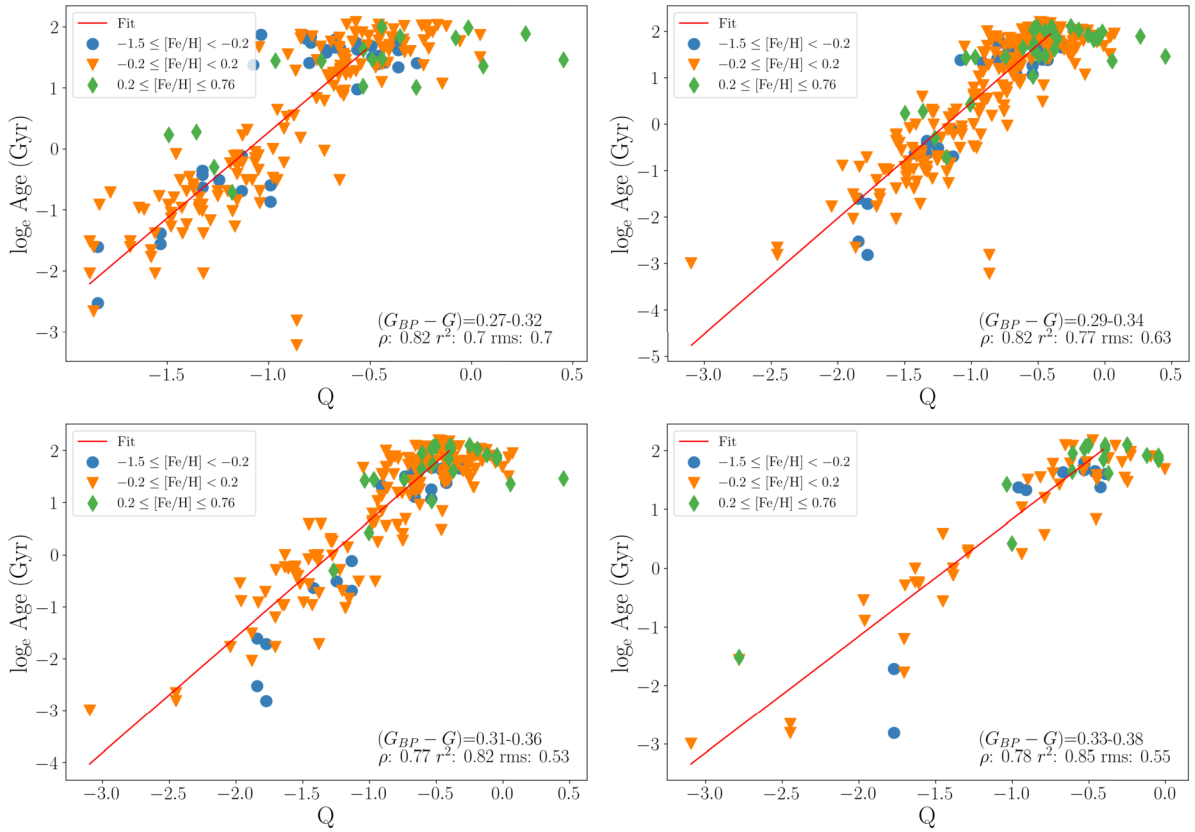

Fig. 3 Literature-reported ages, $\log_e(\tau)$, versus FUV-excess parameter Q. Dwarf stars were divided into *Gaia* $(G_{BP} - G)$ color bins. Four of the eight bins which were constrained are shown as examples. The Spearman's correlation coefficient, ρ, coefficient of determination, r^2, and RMS about $\log_e(\tau)$ for each fit are displayed. The calibration stars were binned into three metallicity ranges: $-1.5 \leq$[Fe/H]< -0.2 (blue circles), $-0.2 \leq$[Fe/H]< 0.2 (orange triangles), and $0.2 \leq$[Fe/H]≤ 0.76 (green diamonds)

correlations between interstellar reddening and the FUV-excess parameter Q within this work. In Crandall et al. (2020), this effect was examined for the calibration between FUV magnitude and Q. Figure 10 of Crandall et al. (2020) shows the residuals of Q about the age-Q calibration fits versus *Gaia* extinction values. They do not observe any significant correlation.

Figure 3 also depicts the metallicity, [Fe/H], values for each dwarf star used in the FUV-age calibration. As described above, these metallicity values were taken from Casagrande et al. (2011) and fall within a range of $-1.5 \leq$[Fe/H]≤ 0.76. The calibration stars were binned into three metallicity ranges and are shown in Fig. 3: $-1.5 \leq$[Fe/H]< -0.2 (blue circles), $-0.2 \leq$[Fe/H]< 0.2 (orange triangles), and $0.2 \leq$[Fe/H]≤ 0.76 (green diamonds). In general, we do not see a clear correlation between metallicity and the FUV-excess parameter Q. That is, for the bins of $-1.5 \leq$[Fe/H]< -0.2 (blue circles) and $-0.2 \leq$[Fe/H]< 0.2 (orange triangles) we see a variety of activity levels as indicated by Q at any given metallicity. However, in the more metal rich population, $0.2 \leq$[Fe/H]≤ 0.76 (green diamonds) we see a shift towards more positive Q values. A more positive Q value correlates with a less active, older star.

We have plotted stellar age, τ, against metallicity [Fe/H] for the calibration sample in Fig. 4. We do not see a major difference in age ranges for the three metallicity bins at least down to a metallicity of about one-tenth solar. The range of age for the metal-rich bin is $0.22 \leq \tau \leq 8.17$. As such, we do not anticipate metallicity to impact the validity of the FUV-age relation for the metal-rich stars. We also note that Fig. 4 shows that the most metal-rich star within the range $-1.5 \leq$[Fe/H]< -0.2 has an age comparable to the Sun.[2] However, low-metallicity stars with ages younger than 3 Gyr are quite rare in the calibration sample, which mostly encompasses what is generally considered, within the literature, near the upper half of the metallicity range of the Galactic thick disk. There are some relatively young ages among some of the most metal-poor stars in Fig. 4. The

[2]The Casagrande et al. (2011) sample flags stars with metallicities that have been obtained outside of the calibration validity range. We investigated the possibility of such stars within our sample. However, after our magnitude and color cuts have been applied to our sample, we find that there are no stars with this flag.

calibration sample does not contain many stars with [Fe/H] metallicities as low as −0.4 dex or less (see Fig. 1), i.e., as low as the Casagrande et al. (2011) survey encompasses. Thus one cannot rule out that at metallicities of < -0.5 dex the age-Q relation might become sensitive to [Fe/H], which could hinder interpreting the apparently young-Q metal-poor stars in Fig. 4.

In the final step of the FUV-age calibration process we investigate how the fit parameters in Table 1 vary with *Gaia* $(G_{BP} - G)$ color. Figure 5 shows $\log_e(a)$ and b parameters versus $(G_{BP} - G)$, where representative colors are the median $(G_{BP} - G)$ within each bin from Table 1. The parameter $\log_e(a)$ is fit with the linear function

$$\log_e(a) = -4.44(G_{BP} - G) + 4.35, \quad (4)$$

and the parameter b is fit by the linear function

$$b = -14.84(G_{BP} - G) + 7.17. \quad (5)$$

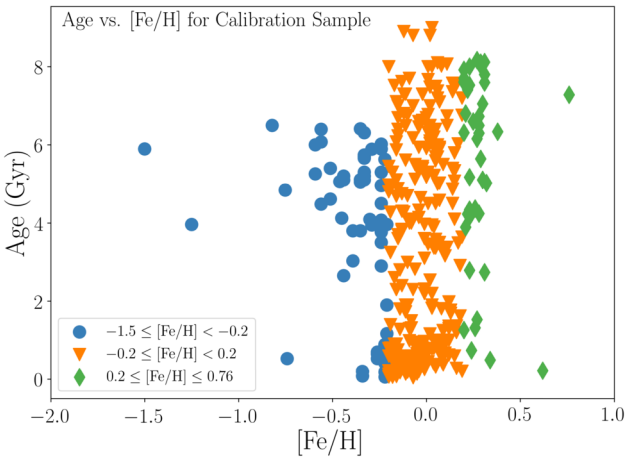

Fig. 4 Stellar age versus [Fe/H] for the calibration sample. Metallicities are from Casagrande et al. (2011)

Errors shown in Fig. 5 are the root-mean sum of the squares of residuals about the determination of each $\log_e(a)$ and b value. With Equations (1) - (5) one can empirically estimate the age of an FGK-type, solar-like star given a *GALEX* FUV magnitude and *Gaia* colors. Alternatively, one may interpolate within a grid of a and b values given in Table 1.

2.3 Related errors

Several factors could contribute to an error in the fits given in Fig. 3 and Table 1, including errors in the age determinations of the calibration stars, metallicity effects, and errors in the FUV magnitude observations. The four sources from which ages were chosen (Lorenzo-Oliveira et al. 2018; Sierchio et al. 2014; Ballering et al. 2013; Isaacson and Fischer 2010) do not have associated errors quoted. As such, we did not include errors for $\log_e(\tau)$ in our analysis. Crandall et al. (2020) explored the possibility of metallicity effects in the FUV-age relation and found no clear correlations. However, they noted that this is potentially the case due to a restricted metallicity range among their calibration stars, which have near-solar abundances. The current calibration also imposes a similar restriction.

The extent to which errors in *GALEX* GR6/7 FUV magnitudes propagate into an age uncertainty were quantified in Sect. 3.3 of Crandall et al. (2020). They concluded that for a 6.0 Gyr solar-type G dwarf there would be an error of ~ 1.0 Gyr in an FUV-derived age, assuming an observational error in FUV magnitude of 0.05 mag. We performed a similar analysis. For a theoretical star of given age between 0-6 Gyr with a solar color of $(G_{BP} - G) = 0.33$ (Casagrande and VandenBerg 2018), we calculated an associated error in the derived FUV-age using Equations (1) - (5) for assumed errors of 0.02 and 0.05 mag in the *GALEX* FUV magnitude. Figure 6 shows the results of these calculations. Here the green dashed line corresponds to a 1:1 exact match in

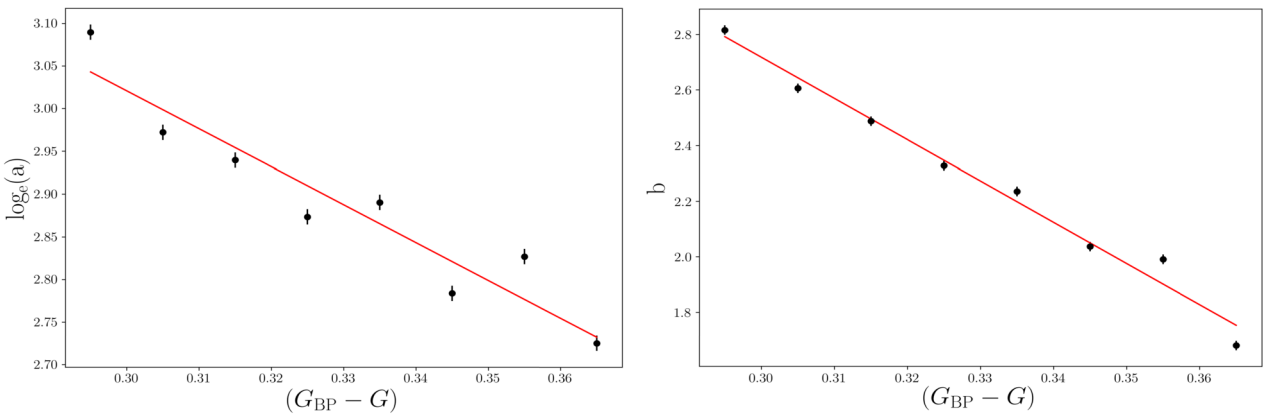

Fig. 5 Fit parameters $\log_e(a)$ and b from Table 1 versus representative $(G_{BP} - G)$ colors. The later are the median values of $(G_{BP} - G)$ within each bin from Table 1. The red lines represent linear fits. Error bars shown are the root-mean sum of the squares of residuals about the determination of each $\log_e(a)$ and b value

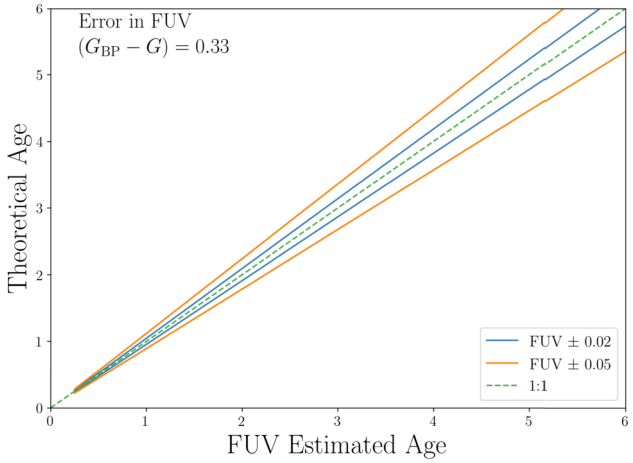

Fig. 6 Estimated errors of FUV-determined ages for a theoretical star with a solar *Gaia* color $(G_{BP} - G) = 0.33$. The green dashed line demonstrates a 1:1 exact match in age, while the blue and orange lines give the age that would be derived for assumed *GALEX FUV* magnitude errors of ±0.02 and ±0.05, respectively

age for no error in FUV magnitude, while the blue and orange lines give the error in derived age for assumed *GALEX FUV* errors of ±0.02 and ±0.05 mag respectively. From Fig. 6 we conclude that for a 6 Gyr star errors in FUV magnitude that are greater than 0.05 mag could translate to an error in derived age of more than 1 Gyr. The FUV magnitude errors, if they amount to 0.05-0.15 mag, can therefore cause large age errors beyond this age threshold. As such, like with Crandall et al. (2020), our calibration is best used for stellar ages less than 6 Gyr.

3 The age-velocity relation

Far-ultraviolet-based ages for FGK dwarf stars can be combined with measurements of their space motions, and applied to a study of correlations between age and kinematics of stars in local regions of the Galaxy. As noted in Sect. 1, the age-velocity relation (AVR) is a general trend which shows that velocity dispersion increases as a function of stellar age within the solar neighborhood. More often than not, an AVR is constructed using isochrone-determined ages. In this section we utilize the Casagrande et al. (2011) sample of thousands of Geneva-Copenhagen Survey dwarf stars to construct an AVR with empirical FUV-determined ages.

3.1 The stellar sample

The basis for the stellar sample which we use to construct an AVR is the Casagrande et al. (2011) collection of solar neighborhood dwarf stars. Casagrande et al. (2011) reanalyzed the Geneva-Copenhagen Survey with new effective temperatures and metallicities (Nordström et al. 2004), which were then used to estimate the ages of FGK type stars with the BASTI (Pietrinferni et al. 2004a,b, 2009) and Padova (Bertelli et al. 2008, 2009) isochrone models.

The GCS sample was comprised of 12,329 dwarf stars. We then discarded stars that do not have *GALEX FUV* or *Gaia G* and G_{BP} magnitudes. Additionally, stars without *Gaia* parallax measurements were omitted, as this information is used to make an absolute magnitude cut on the sample. The FUV-age calibration in Sect. 2 is only functional for stars with absolute magnitudes $4.3 \leq M_V \leq 5.3$. As such, we did not include stars outside of this solar-analog range. Absolute visual magnitudes for each star were determined by

$$M_V = V + 5.0(1.0 + \log_{10} p), \tag{6}$$

where V is the Johnson magnitude and p is the parallax in arc sec. The FUV-age calibration is also restricted by the Johnson color range $0.55 \leq (B - V) \leq 0.71$ and *Gaia* color range $0.24 \leq (G - G_{BP}) \leq 0.39$, and stars outside of these ranges were not included in the sample. The final magnitude and color-cut sample contained 660 dwarf stars.

3.2 An AVR with literature-reported ages

We first constructed a baseline AVR, Fig. 7, with the Casagrande et al. (2011) sample without performing any of the color, magnitude or metallicity cuts mentioned above. The ages in this figure are determined by Casagrande et al. (2011) with Padova isochrones in which a probability distribution was constructed using a Bayesian framework and a median value is the final derived age (see Appendix A of Casagrande et al. 2011).

Each of the three velocity dispersions were constructed from the 3D velocity components UVW, which were also quoted in Casagrande et al. (2011) and measured in the Geneva-Copenhagen Survey (Nordström et al. 2004). To determine the velocity dispersion in a given axis we first binned the 12,329 stars by age in bin width of 0.5 Gyr from 0-10 Gyr. We then utilized the median absolute deviation (MAD) to determine dispersions σ_U, σ_V, and σ_W. For example,

$$\sigma_U = \text{median}|U_i - \tilde{U}| \tag{7}$$

where U_i is a given star's U velocity and $\tilde{U}$ is the median velocity for a given bin. Within each bin we use a median representative age, $\tilde{\tau}$. The first three panels in Fig. 7 show the MAD velocity dispersions for the three kinematic components versus median isochrone age. We also constructed a final AVR represented by a dispersion which we denote s. This dispersion is a quadrature sum of the U, V, and W velocity dispersions:

$$s = \sqrt{\sigma_U^2 + \sigma_V^2 + \sigma_W^2}. \tag{8}$$

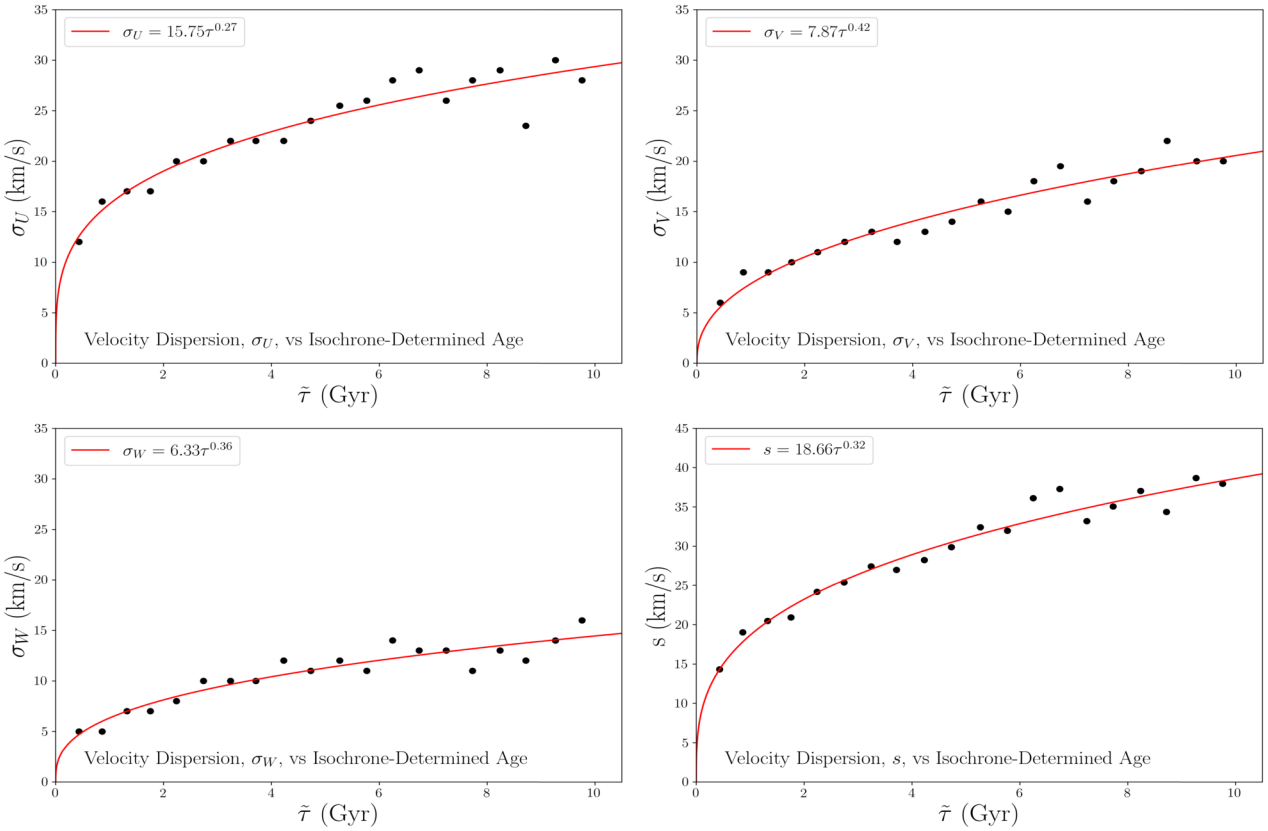

Fig. 7 Age versus velocity dispersion plots derived using data from the Casagrande et al. (2011) sample of 12,329 dwarf stars. No metallicity, color, or magnitude cuts were made to this sample. Velocity dispersions for UVW were determined using the median absolute deviation, and ages were determined with Padova isochrones. A median age, $\tilde{\tau}$ was determined for each bin. The combined velocity dispersion, s, is the quadrature sum of the UVW velocity dispersions. Each relation is fit by a power law function (red)

The s values are shown versus median isochrone age, $\tilde{\tau}$, in the bottom right panel of Fig. 7. Again, this AVR represents the constructed Casagrande et al. (2011) relation using their data without color, magnitude, or metallicity cuts made to the sample. The shape of this AVR is comparable to that of Fig. 17 in Casagrande et al. (2011). Errors are not shown in Fig. 7 as UVW velocity errors are not given in the Casagrande et al. (2011) sample.

Traditionally, an AVR is fit with a power law function and we have done so in each panel in Fig. 7, represented by the red curve. The fits are defined as

$$\sigma_U = 15.75\tau^{0.27}, \tag{9}$$

$$\sigma_V = 7.87\tau^{0.42}, \tag{10}$$

$$\sigma_W = 6.33\tau^{0.36}, \tag{11}$$

and

$$s = 18.66\tau^{0.32} \tag{12}$$

where τ is the Padova isochrone-determined age in Gyr and the velocity dispersions are in units of km s^{-1}. The root-mean-square (RMS) residuals about the velocity dispersion fits are 1.52, 1.15, 1.00, and 1.37 km s^{-1} for σ_U, σ_V, σ_W, and s, respectively. These fits are noted in Table 2.

3.3 An AVR with FUV-determined ages

The stellar age-dating tool developed in Sect. 2, in which we calibrated a relationship between *GALEX* FUV magnitudes and age, is useful because it is a purely empirical relationship. Hence, this tool uniquely compliments other age-dating techniques based on isochrones, since it is largely based upon the time dependence of stellar activity.

We have taken the compilation of Casagrande et al. (2011) dwarf stars with the absolute magnitude and color cuts described in Sect. 3.1 and estimated their ages with *GALEX* FUV observations. Equations (1) - (5) were used to determine the FUV age, τ, for each of the 660 stars in the resulting sample.

The stars were then binned by age in order to determine a MAD representative value of the velocity dispersion components. However, in this case, the sample was reduced from the original 12,329 Casagrande et al. (2011) stars to 660 after color and magnitude cuts. As such, there were significantly fewer stars older than ~ 4 Gyr in the FUV sample.

Table 2 Power law fits to age *vs.* velocity dispersion relations

Age determination[a]	Velocity determination[b]	Velocity dispersion	a[c]	β[c]	RMS[d] km s^{-1}
Isochrone	GCS	σ_U	15.75±0.66	0.27±0.02	1.52
Isochrone	GCS	σ_V	7.87±0.47	0.42±0.03	1.15
Isochrone	GCS	σ_W	6.33±0.42	0.36±0.04	1.00
Isochrone	GCS	s	18.66±0.59	0.32±0.02	1.37
Isochrone	GCS with color cuts[e]	s	18.56±1.46	0.23±0.05	2.87
FUV	GCS	σ_U	16.44±1.25	0.21±0.05	3.16
FUV	GCS	σ_V	10.94±1.25	0.24±0.08	3.12
FUV	GCS	σ_W	7.10±0.99	0.34±0.09	2.41
FUV	GCS	s	21.28±0.84	0.24±0.03	2.10
Isochrone	*Gaia*	σ_U	16.23±0.76	0.28±0.03	1.76
Isochrone	*Gaia*	σ_V	7.86±0.77	0.44±0.05	1.91
Isochrone	*Gaia*	σ_W	6.02±0.33	0.42±0.03	0.80
Isochrone	*Gaia*	s	18.91±0.70	0.34±0.02	1.65
FUV	*Gaia*	σ_U	15.90±1.11	0.21±0.05	2.82
FUV	*Gaia*	σ_V	11.64±1.18	0.29±0.07	3.02
FUV	*Gaia*	σ_W	7.48±1.13	0.31±0.10	2.75
FUV	*Gaia*	s	21.48±0.98	0.21±0.03	2.47

[a]The method used to determine ages. Isochrone ages are quoted in Casagrande et al. (2011) and FUV ages are estimated using the calibration in Sect. 2

[b]GCS velocities quoted in Casagrande et al. (2011) are taken from the Geneva-Copenhagen Survey, while *Gaia* velocities were determined here from *Gaia* proper motions, parallaxes, and radial velocities

[c]Power-law fit parameters of the form $\sigma = a\tau^{\beta}$ with τ in Gyr and velocity dispersions in km s^{-1}

[d]RMS scatter about the velocity dispersion fit

[e]This AVR was constructed with Casagrande et al. (2011) ages and velocities, but only consisted of stars with $4.3 \leq M_V \leq 5.3$, Johnson color $0.55 \leq (B-V) \leq 0.71$, and *Gaia* color $0.24 \leq (G-G_{BP}) \leq 0.39$

We accounted for this by using varying bin widths. Velocity dispersions σ_U, σ_V, σ_W, and s were calculated in the same manner as the full Casagrande et al. (2011) sample.

Figure 8 shows all age-velocity relations when utilizing FUV-determined ages. We note more scatter compared to Fig. 7 for stars older than ~ 4 Gyr. Additionally, the velocity dispersion relation in the V component is flatter than the full Casagrande et al. (2011) sample. We also note that the FUV-age relationship is best for stars younger than ~ 6 Gyr, as an estimated associated FUV error is 1 Gyr for a 6 Gyr old star. Each dispersion relation was fit with a power law function:

$$\sigma_U = 16.44\tau^{0.21}, \tag{13}$$

$$\sigma_V = 10.94\tau^{0.24}, \tag{14}$$

$$\sigma_W = 7.10\tau^{0.34}, \tag{15}$$

and

$$s = 21.28\tau^{0.24}, \tag{16}$$

where τ is the *GALEX* FUV-determined age in Gyr and velocity dispersions are again in km s^{-1}. The RMS values about the velocity dispersion fits are 3.16, 3.12, 2.41, and 2.10 km s^{-1} for σ_U, σ_V, σ_W, and s, respectively. Power law fit parameters for these AVRs are listed in Table 2.

To compare the FUV-age AVR and literature-age AVR, we constructed an additional AVR which uses Casagrande et al. (2011) velocities and ages, as in Sect. 3.2, but places color and magnitude constraints on the sample. We used the color ranges previously noted in Section 3.2. These constraints reduced the sample to 1,066 stars. Figure 9 shows the AVR constructed with Casagrande et al. (2011) ages and a quadrature sum of the 3D velocity dispersions, s. As in the previous AVR plots, stars were binned and a MAD representative velocity dispersion was calculated for each bin. This AVR was fit to a power law:

$$s = 18.56\tau^{0.23}, \tag{17}$$

which is also given in Table 2. The power law parameter, $\beta = 0.23$, for this AVR is comparable to that of the FUV-

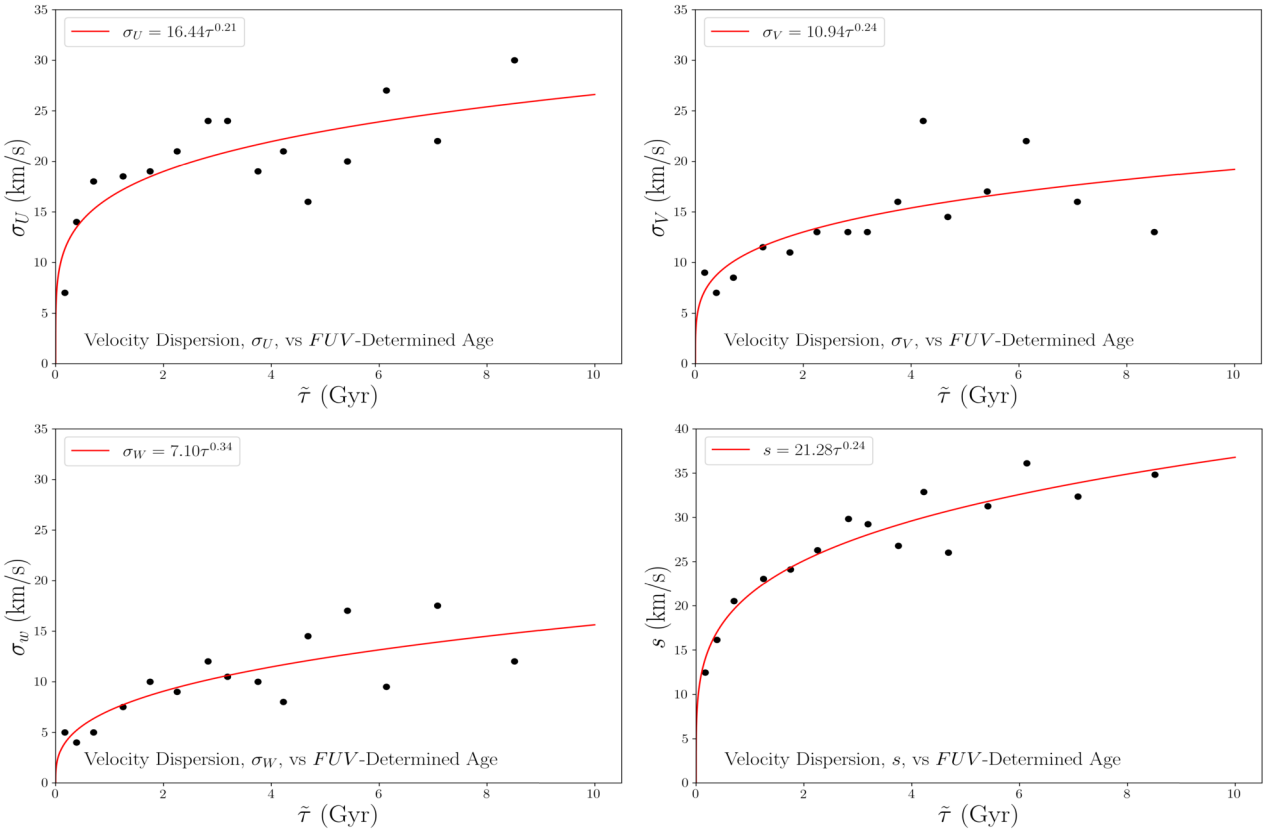

Fig. 8 Age-velocity relations for the Casagrande et al. (2011) sample with magnitude and color-cuts (660 stars) and FUV-determined ages. A median age, $\tilde{\tau}$, was determined for each bin. Velocity dispersions for UVW were determined using the median absolute deviation. The combined velocity dispersion, s, is the quadrature sum of the UVW velocity dispersions. Each relation is fit by a power law function (red)

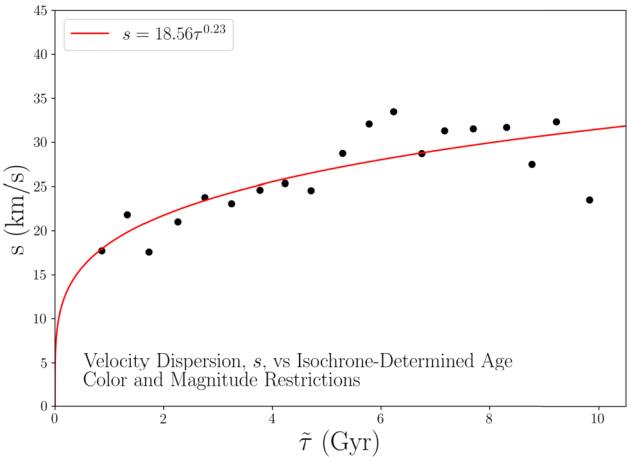

Fig. 9 Age *vs.* velocity dispersion plot for the Casagrande et al. (2011) sample with magnitude and color-cuts (1,066 stars) and literature-reported ages. $\tilde{\tau}$ is the median age within each bin. The combined velocity dispersion, s, is the quadrature sum of the UVW velocity dispersions. The relation is fit by a power law function (red)

age AVR, $\beta = 0.24$. One possibility for the similar fit is that stars within the solar-like range tend to have a flatter AVR with a $\beta \sim 0.23 - 0.24$. Another possibility is that the reduced number of stars has resulted in a flatter AVR.

3.4 AVRs with *Gaia*-determined velocities

An additional step in constructing age-velocity relations was to determine the 3D velocities of the Casagrande et al. (2011) sample by using *Gaia* kinematic information. We compiled a sample of Casagrande et al. (2011) stars with RA, DEC, proper motions, radial velocities, and parallax observations from the *Gaia* Data Release 2, yielding data for a total of 11,350 stars. The UVW velocity components were determined by inputting the *Gaia* kinematics into the PyAstronomy package (Czesla et al. 2019).

Figure 10 shows the UVW velocity components derived from the *Gaia* data plotted against velocities quoted in the Casagrande et al. (2011) data set. The red line represents an equivalent velocity between the two samples. Velocity components in all three directions are quite similar and there is little systematic difference between Casagrande et al. (2011) and *Gaia* velocities. The root mean square deviations for the U, V, and W components are 5.28, 4.75, and 4.11 km s^{-1} respectively.

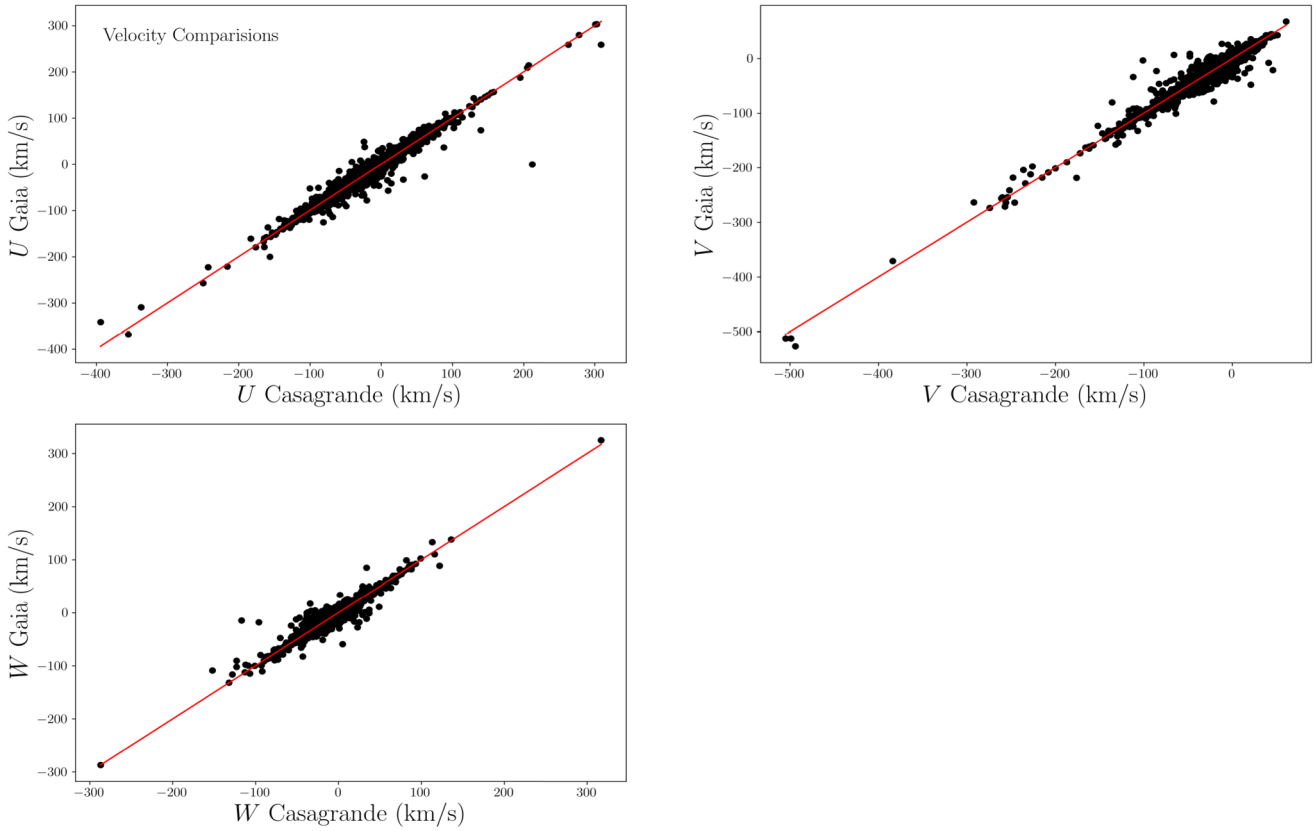

Fig. 10 Space velocity components UVW as derived from *Gaia* data versus velocities for the same stars quoted in the Casagrande et al. (2011) data set. The red line represents an equivalent velocity between the two samples

We did not perform magnitude or color cuts on this collection of 11,350 stars before constructing an AVR. The AVR plots for the Casagrande et al. (2011)-*Gaia* cross-matched sample are shown in Fig. 11. Again, the velocity dispersions were determined by *Gaia* velocities and the stellar ages come from Casagrande et al. (2011) isochrone fitting. As before, the AVRs were fit with a power law function:

$$\sigma_U = 16.23\tau^{0.28}, \tag{18}$$

$$\sigma_V = 7.86\tau^{0.44}, \tag{19}$$

$$\sigma_W = 6.02\tau^{0.42}, \tag{20}$$

and

$$s = 18.91\tau^{0.34} \tag{21}$$

where τ is the Padova isochrone-determined age in Gyr and velocity dispersions are again in km s^{-1}. The RMS deviations about the velocity dispersion fits are 1.76, 1.91, 0.80, and 1.65 km s^{-1} for σ_U, σ_V, σ_W, and s, respectively. The fits and RMS values are also given in Table 2. The RMS deviations are smaller than for the fits to the Casagrande et al. (2011) velocity-determined sample.

Finally, we have constructed AVR plots using *Gaia*-determined velocities and FUV-determined ages. All four velocity dispersions are shown versus stellar age in Fig. 12 along with the power law fit to each relation. Similar to the AVR in Fig. 8, this sample only includes stars with *GALEX* FUV magnitudes, colors within $0.55 \leq (B-V) \leq 0.71$ and $0.24 \leq (G - G_{BP}) \leq 0.39$, and absolute magnitudes within the range $4.3 \leq M_V \leq 5.3$; a total of 598 stars. Each plot was fit with a power law function:

$$\sigma_U = 15.90\tau^{0.21}, \tag{22}$$

$$\sigma_V = 11.64\tau^{0.19}, \tag{23}$$

$$\sigma_W = 7.48\tau^{0.31}, \tag{24}$$

and

$$s = 21.48\tau^{0.21} \tag{25}$$

where τ is the FUV-determined age in Gyr. The RMS values about the velocity dispersion fits are 2.82, 3.02, 2.75, and 2.47 km s^{-1} for σ_U, σ_V, σ_W, and s, respectively. The relations shown in Fig. 12 are not as clearly defined as in Fig. 11. This is likely a consequence of a lower number of

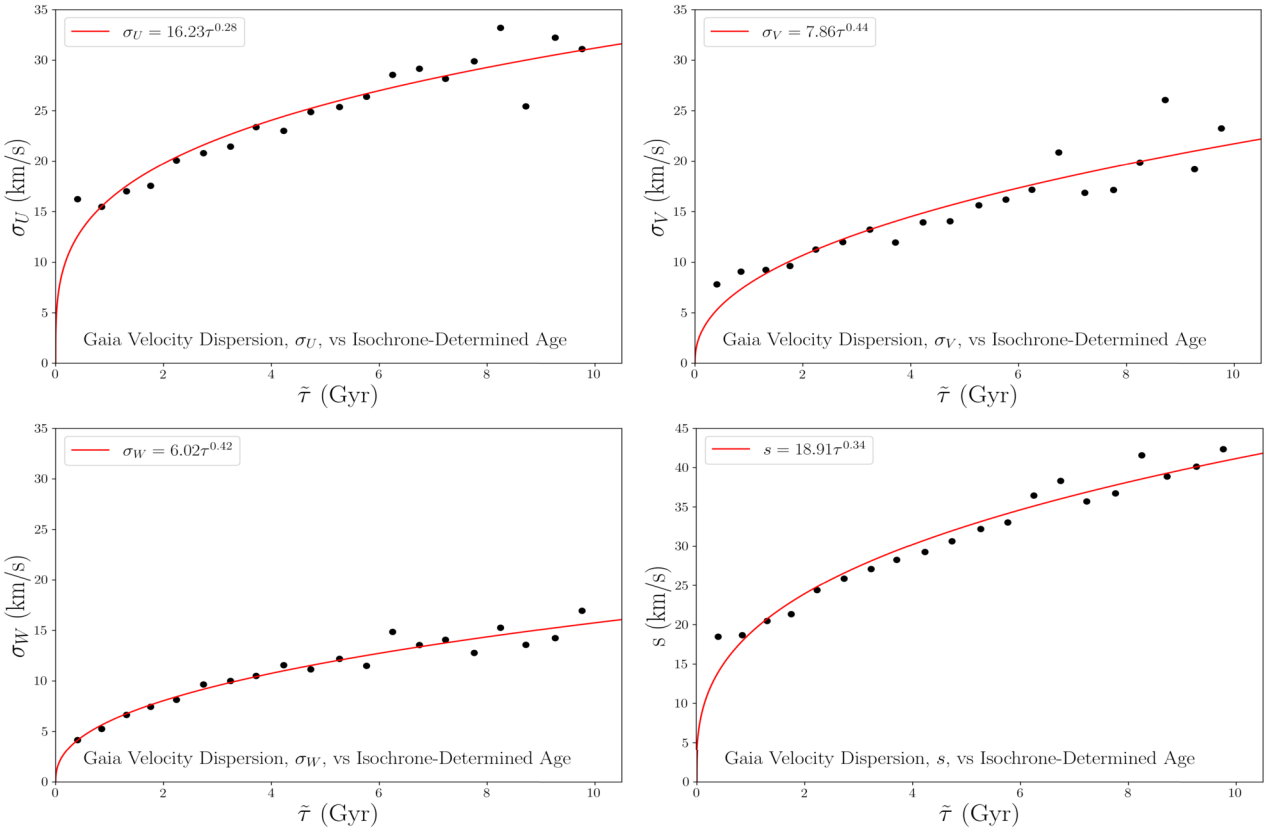

Fig. 11 Age-velocity relation plots for the Casagrande et al. (2011) sample using isochrone-determined ages and *Gaia*-derived velocity dispersions. Velocity dispersions for the UVW components were determined using the median absolute deviation. $\tilde{\tau}$ is the median age within each bin. The combined velocity dispersion, s, is the quadrature sum of the UVW components. The AVR relation is fit by a power law function (red)

stars in this sample as compared to that in Fig. 11. We note that there are no significant differences in power law fits when comparing the Casagrande et al. (2011) and *Gaia* velocities. For example, the value of β found when fitting the s-AVR with isochrone-determined ages and GCS velocities is 0.32 ± 0.02. This is comparable to $\beta = 0.34 \pm 0.02$, which describes the fit of the s-AVR constructed with isochrone-determined ages and *Gaia* velocities. Likewise, the FUV-age versus s AVR with GCS velocities is fit with $\beta = 0.24 \pm 0.03$, which is comparable to $\beta = 0.21 \pm 0.03$ that describes the s-AVR with FUV-determined ages and *Gaia* velocities.

3.5 Comments on the age-velocity relations

Holmberg et al. (2009) simulated AVRs using synthetic Geneva-Copenhagen Survey observations. They show in their Fig. 8 (panel a) that if only GMCs or other local heating agents contributed to heating, the AVR would continuously rise in velocity dispersion. Our AVR Fig. 8, as well as that constructed with Casagrande et al. (2011) velocities and ages (Fig. 7), show a flattening of the curve around 2-3 Gyr. Holmberg et al. (2009) further demonstrated in panels c and d of their Fig. 8, that a minor merger occurring at the 3 Gyr mark would cause such a flattening. It is quite possible that our observational AVRs are indeed showing the results of the Milky Way experiencing an early minor merger.

The power law fit parameter, β, gives insight into the formation history of the Milky Way. Ting and Rix (2019) argue that many solar-neighborhood studies agree that the velocity dispersion towards the North Galactic pole, σ_W, fit with a power law results in a parameter $\beta \sim 0.5$. However, simple simulations of an AVR created solely by heating due to Giant Molecular Clouds (GMCs) have resulted in a fit parameter of $\beta \sim 0.25$ (Hänninen and Flynn 2002; Kokubo and Ida 1992). Additionally, Spitzer and Schwarzschild (1951) who first highlighted such a relation, found their mean velocity dispersion was fit to a function with $\beta = 1/3$. Indeed, there are differences in the shapes of simulated AVRs. One heating mechanism alone may not be enough to describe velocity dispersion observations. There may very well be several mechanisms which play a role. In our work, we created AVRs with Casagrande et al. (2011) isochrone-determined ages, and found a $\beta \sim 1/3$ (see Table 2). Our observational AVRs which were constructed with a sample of stars with solar-like colors and magnitudes were fit with a $\beta \sim 0.23$.

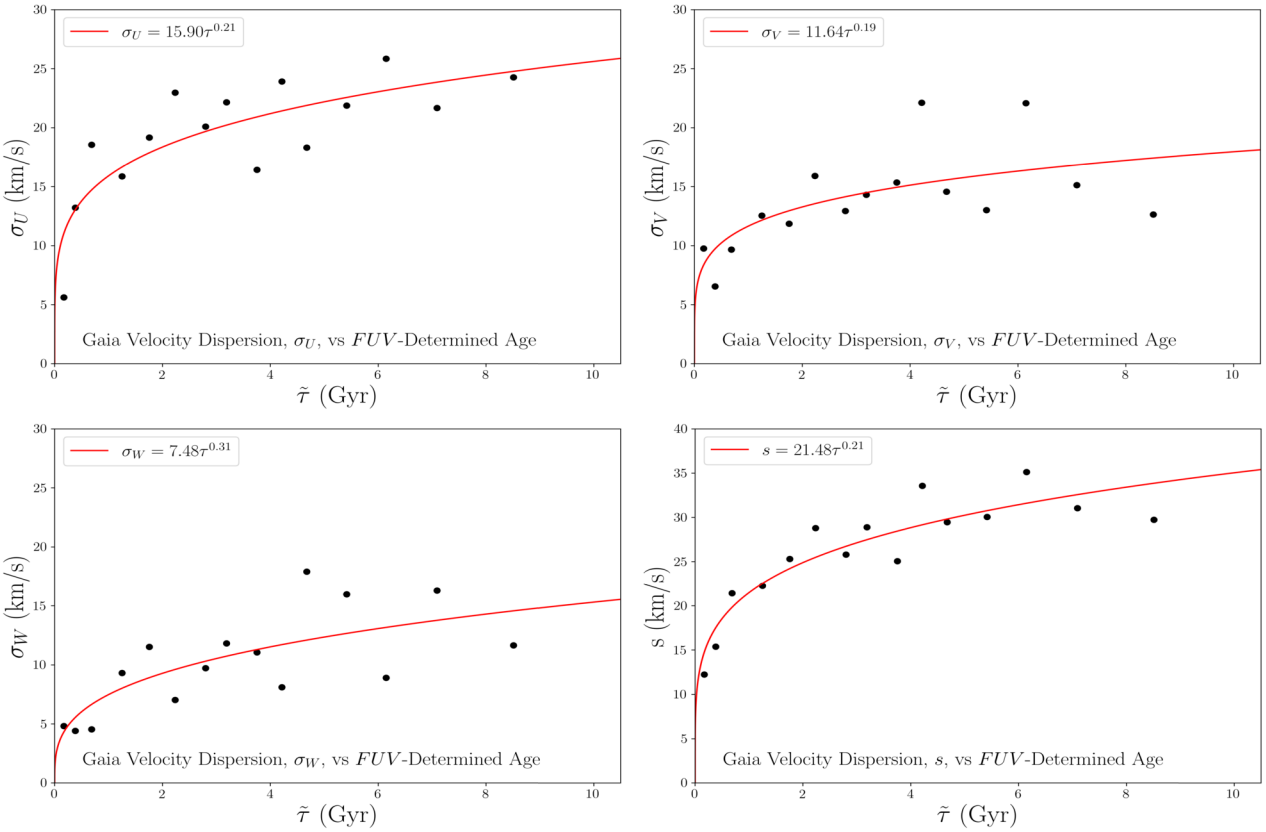

Fig. 12 Age-velocity relation plots for the Casagrande et al. (2011) sample FUV-determined ages and *Gaia*-derived velocity dispersions. Velocity dispersions for the UVW components were determined using the median absolute deviation. $\tilde{\tau}$ is the median age within each bin. The combined velocity dispersion, s, is the quadrature sum of the UVW velocity dispersions. The relation is fit by a power law function (red)

There are many reasons as to why observational AVRs may not be consistent with those in simulations. This includes the variance in methods for age-dating stars and the constraints of local data certainly impact our interpretations of the age-velocity relation.

4 Stellar metallicity, chromospheric activity, age, and orbit parameters

Similar to the AVR, the age-metallicity relation (AMR) is often used to interpret the formation history of the Milky Way. Twarog (1980a,b) found an age-metallicity relationship (AMR) for nearby main sequence stars within the Milky Way which has since been used to test chemical evolution hypotheses. This work on the Solar neighborhood AMR has been greatly extended by the Geneva-Copenhagen Survey (Casagrande et al. 2011; Holmberg et al. 2007, 2009). The common consensus of the Milky Way's disk structure is that it consists of younger stars which reside closer to the Galactic plane and tend to be more metal-rich, while older stars are more vertically dispersed and metal-poor. Thus, as noted in the previous section, the limitations of a local sample of stars for studying the AVR of the Galactic disk also apply to the age-metallicity relation, which can also vary with position in the Galaxy.

Quite often the population of stars in the Milky Way disk are split into two groups: thin and thick disk constituents. The formation histories of these two populations have received much discussion in the literature, with Bird et al. (2013) providing a detailed discussion. In one general scenario the thick disk is considered to have formed in situ when metal-poor stars maintained their orbital scale heights after formation and the surrounding gas collapsed into the Galactic plane (Veltx et al. 2008; Robin et al. 2014; Navarro et al. 2018). Thin disk stars may have then formed later in the collapsed gas disk. Alternatively, perhaps a major merger (Veltx et al. 2008), or several mergers (Brook et al. 2004), early on in the Milky Way's formation history formed the thick disk stars via accretion. As suggested in the previous section, our Galaxy's current structure may have been the result of heating mechanisms which have driven the thick disk outwards ("inside out" formation). As these thick disk stars are older, they have had more opportunities to gravitationally interact with Giant Molecular Clouds (Hänninen and Flynn 2002; Aumer et al. 2016), black holes (Lacey and

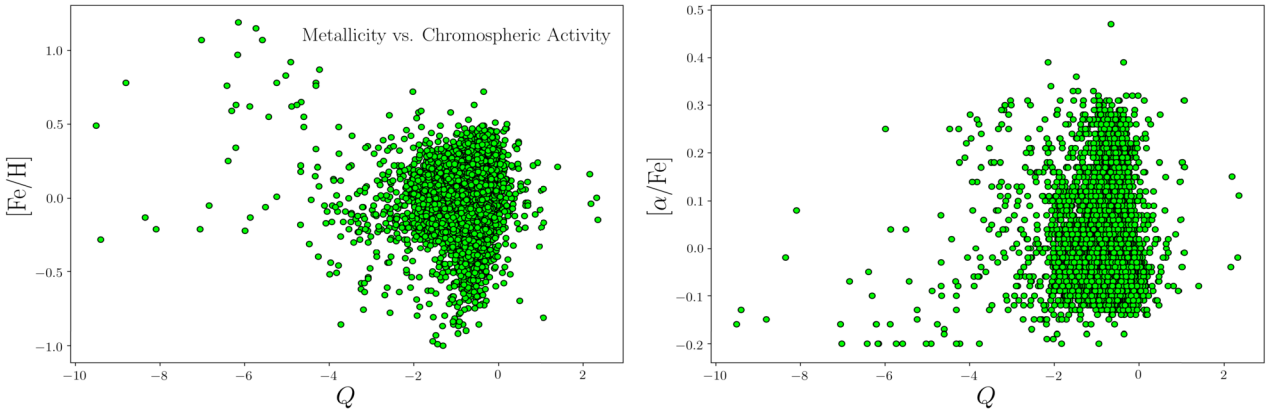

Fig. 13 Metallicity [Fe/H] and [α/Fe] from Casagrande et al. (2011) as a function of chromospheric activity indicator Q

Ostriker 1985; Hänninen and Flynn 2002) and other stars.[3] Many works support the claim that within the varying scenarios of mechanisms which have driven the Milky Way's evolution, the kinematic trends were likely designated at birth (Bird et al. 2013). Regardless of the formation history, the thin and thick disk stars have often been classified by their [Fe/H] abundance, age, or a combination of the two parameters.

However, there is significant, recent interest in a different classification of stellar populations based on [α/Fe] abundance ratios. High α-abundance and low-α stars then distinguish the high- and low-α disks, respectively, within the solar neighborhood (Fuhrmann 1998; Prochaska et al. 2000), and this concept has been extended to Galactic structure studies (Bovy et al. 2012; Haywood et al. 2013; Bovy et al. 2016). It is important to note that Bovy et al. (2012) found a lack of clear correlation between the low-α and high-α disks and the thin and thick disks. In addition, the distinction between low-α and high-α disks appears to be dependent upon Galactocentric radius, where the high-α population resides closer to the Galactic center and the low-α population in an annulus further out (Bovy et al. 2016; Haywood et al. 2016; Mackereth et al. 2019).

Table 3 Average activity indicator Q in metallicity and [α/Fe] bins

[α/Fe] Bin	$\langle Q \rangle$	$\langle$[α/Fe]$\rangle$
−0.2 to − 0.1	−0.73	−0.11
−0.1 to 0.0	−0.65	−0.03
0.0 to 0.1	−0.73	0.06
0.1 to 0.2	−0.76	0.15
0.2 to 0.3	−0.61	0.24
[Fe/H] Bin	$\langle Q \rangle$	$\langle$[Fe/H]$\rangle$
−0.9 to − 0.8	−1.16	−0.81
−0.8 to − 0.7	−0.75	−0.73
−0.7 to − 0.6	−0.72	−0.63
−0.6 to − 0.5	−0.51	−0.52
−0.5 to − 0.4	−0.65	−0.45
−0.4 to − 0.3	−0.54	−0.33
−0.3 to − 0.2	−0.83	−0.23
−0.2 to − 0.1	−0.78	−0.15
−0.1 to 0.0	−0.70	−0.05
0.0 to 0.1	−0.70	0.05
0.1 to 0.2	−0.53	0.15
0.2 to 0.3	−0.53	0.24
0.3 to 0.4	−0.66	0.36

4.1 Age-metallicity relation

We explored a possible AMR for our sample of stars by first investigating the relationship between metallicity and the chromospheric activity indicator Q. Values of the metallicity [Fe/H] and [α/Fe] used here are from Casagrande et al. (2011), who derived a new metallicity scale for the Geneva-Copenhagen Survey sample of Solar neighborhood stars. These metallicity estimates are not accompanied with errors within the Casagrande et al. (2011) catalog. We only considered stars from the sample which have *GALEX* FUV observations. In addition, stars were only considered if they fell within the *Gaia* color range $0.27 < (G_{BP} - G) < 0.40$, as this range reveals the variance of chromospheric activity within the FUV broadband range without significant photospheric contamination. This sub-sample consisted of 4,644 stars. Activity indicator, Q, estimates were derived for each of the stars using Equations (2) and (3).

Figure 13 shows the Casagrande et al. (2011) metallicity [Fe/H] and [α/Fe] versus the FUV-based chromospheric activity indicator Q. A comparison of Fig. 13 to Fig. 16 of Casagrande et al. (2011) (their age-metallicity relationship) shows that for stars with metallicity $-0.5 \lesssim$ [Fe/H] $\lesssim 0.5$,

[3] Although the assembled mass from GMCs and black holes contributes to the scattering significantly more than stellar mass.

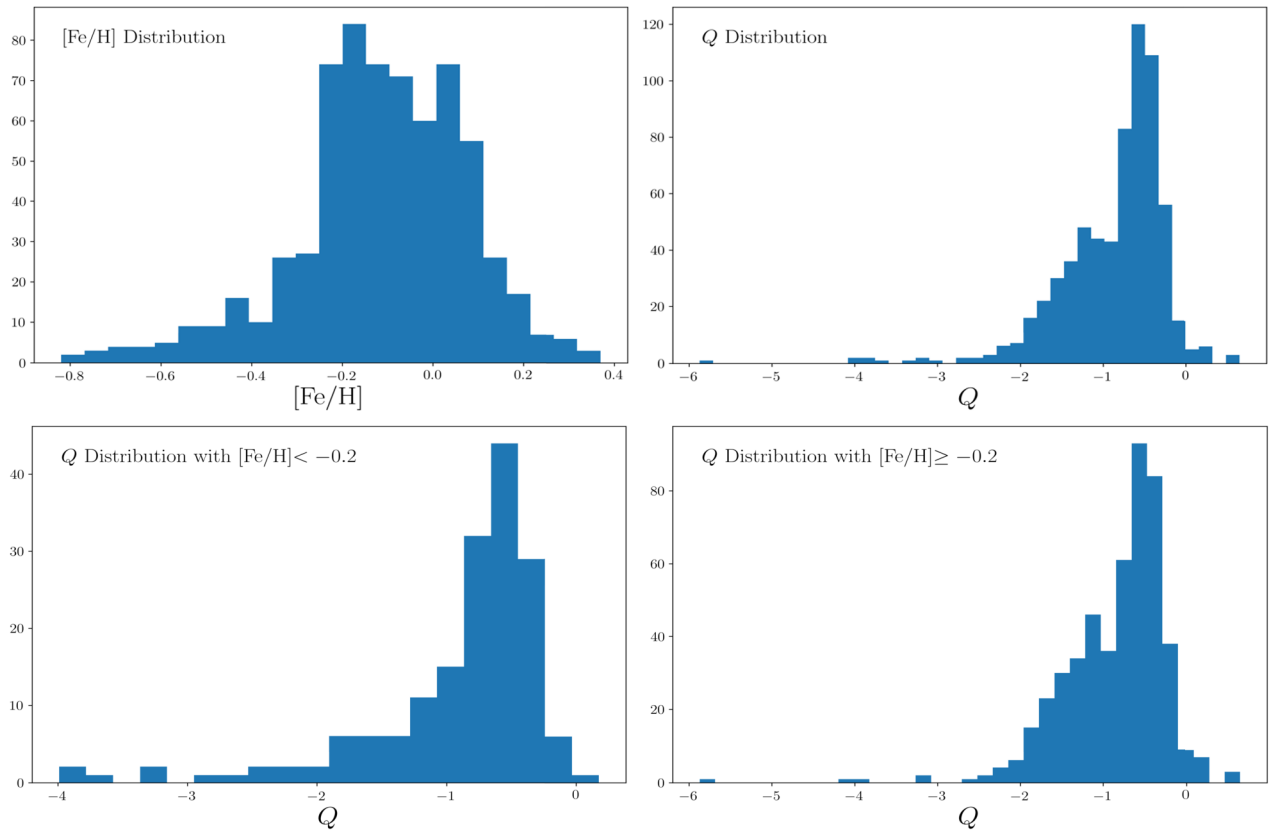

Fig. 14 Distributions of the metallicity [Fe/H] and chromosphere activity indicator Q for stars in the combined GCS-*GALEX* sample. The top-left panel shows the distribution of metallicity for all stars in the sample for which we have derived FUV ages. The top-right panel shows the chromospheric activity indicator, Q, distribution for this sample of stars. The bottom panels have divided the stars into two populations as regards metallicity: [Fe/H]< -0.2 (left) and [Fe/H]≥ -0.2 (right)

there is a wide distribution of both age and activity levels. Furthermore, among stars with [FeH] < -0.5 the spread in Q is less than among the more metal-rich stars.

In Fig. 13 we see that chromospherically inactive stars (those with more positive Q) have a wide metallicity range. As such, we are left with the question of whether there is a correlation between activity parameter Q and metallicity. This is explored in Fig. 14. The top-left panel shows the distribution of metallicity for all stars in the sample for which we can derive FUV-ages. The top-right panel shows the distribution of the chromospheric activity indicator, Q, for this sample of stars. The bottom panels distinguish between the stars with [Fe/H]< -0.2 (left) and [Fe/H]≥ -0.2 (right). We performed a two-sample KS test between the two bottom panels and found a p-value of 0.38. We cannot reject the null hypothesis that the distributions of the two samples are the same since the p-value is high. There is no significant difference in the distributions of Q between these two metallicity populations. We further explored the relationship between Q and metallicity by binning the stars in both [Fe/H] and [α/Fe] by 0.1 dex and finding the average Q within each bin. The results of this binning are shown in Table 3, and they reveal that there is little, if any, relationship between the mean value of Q and either [Fe/H] metallicity or [α/Fe] for this sample of stars.

An age for each star in the *GALEX*-GCS sample was determined using Equations (1), (4), and (5). These ages are shown plotted against both metallicity [Fe/H] and [α/Fe] in the left and right panels of Fig. 15 respectively. Similar to Fig. 16 of Casagrande et al. (2011), there appears to be little to no correlation between metallicity and age in this figure. It must be noted, however, that the oldest ages plotted in Fig. 15 represent an extrapolation of our age calibration.

4.2 Stellar age and orbit parameters

In addition to kinematic information, Casagrande et al. (2011) also provide orbit information for the GCS stars, including the perigalactic radius ($r_{\rm min}$), apogalactic radius ($r_{\rm max}$), and orbit eccentricity derived thereby. Figure 16 shows each of these orbit parameters as a function of *GALEX* FUV-determined ages. Interestingly, Fig. 16 suggests that some stars of age > 3 Gyr may not have formed in the solar neighborhood. There is a tendency for stars of such age with high eccentricity to have small perigalactic radii.

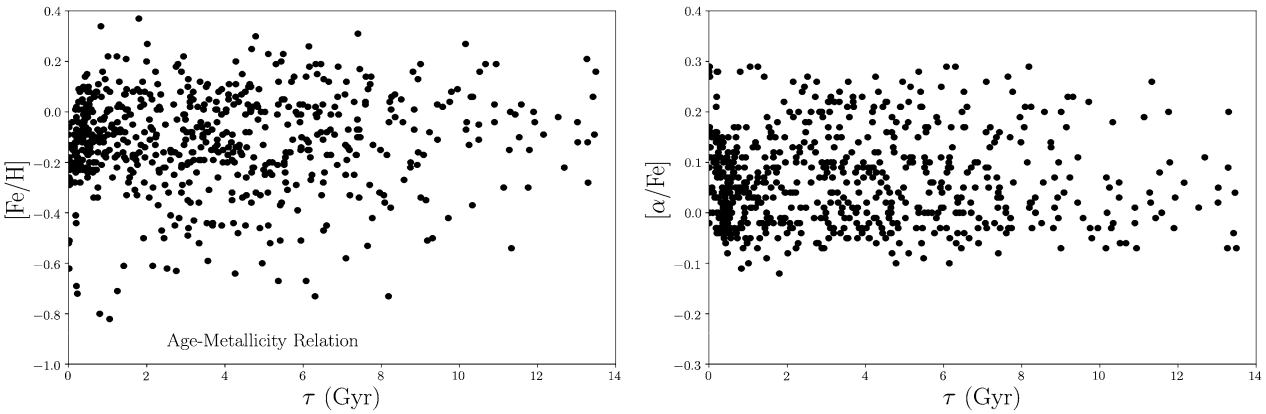

Fig. 15 Age-metallicity plot for stars with FUV-determined ages and metallicities from Casagrande et al. (2011)

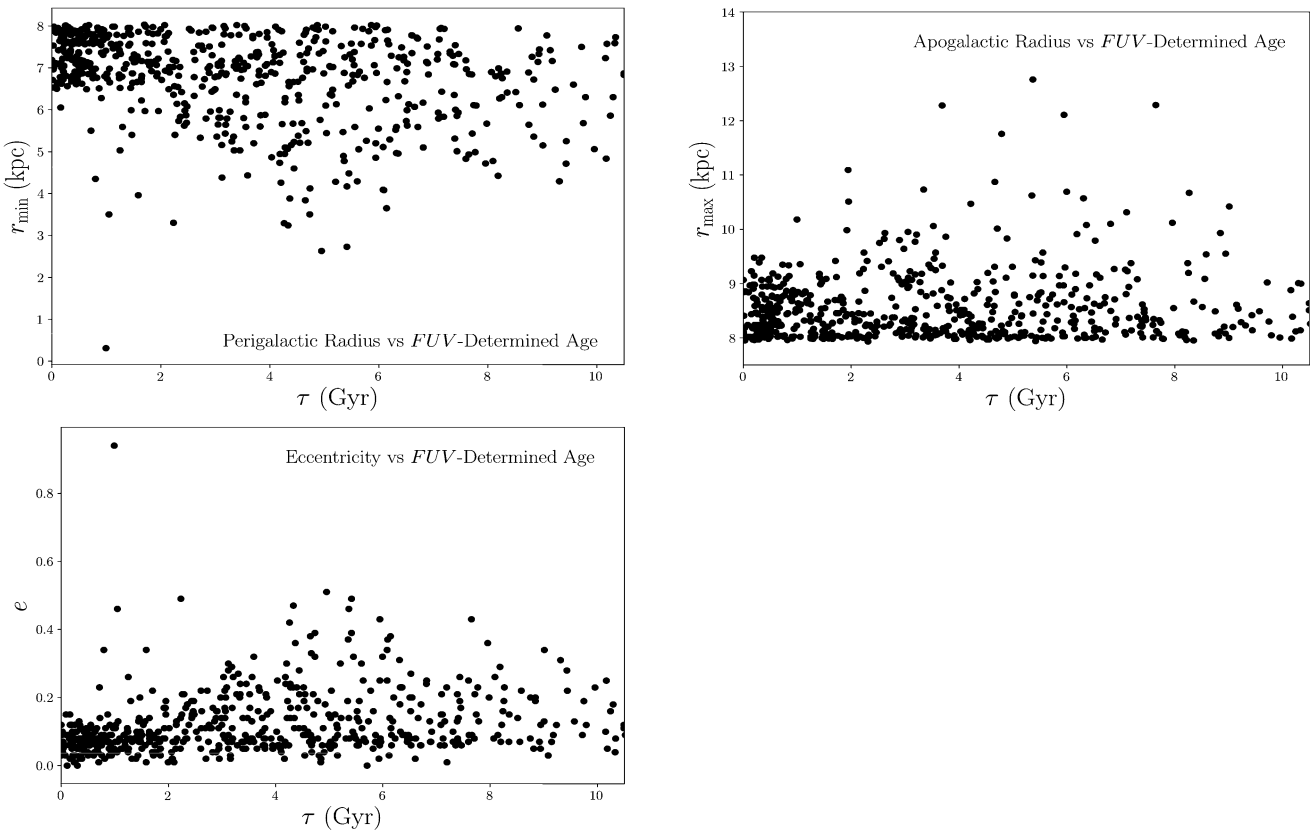

Fig. 16 Perigalactic radius (r_{min}), apogalactic radius (r_{max}), and orbit eccentricity given by Casagrande et al. (2011) as a function of FUV-determined ages (τ)

To further investigate this pattern, the age-metallicity plots of Fig. 15 have been recreated for four different populations of stars: two populations selected with $r_{min} < 6.0$ kpc and $r_{min} \geq 6.0$ kpc (Fig. 17), and two populations sorted by eccentricity at $e < 0.2$ and $e \geq 0.2$ (Fig. 18). Both Figures show [Fe/H] and [α/Fe] against FUV-determined ages. These figures demonstrate that the population of stars with high orbit eccentricity and small perigalactic radii are not young. Very few stars with $r_{min} < 6.0$ kpc formed in the last 2 billion years. In addition, the mean [Fe/H] for stars with $e \geq 0.2$ is smaller than stars with smaller eccentricity.

Older stars with low metallicity, large orbit eccentricity, and small perigalactic radii are consistent with a Galactic model that includes radial mixing by dynamical heating. Here, the inner parts of the Milky Way formed first, and the first-formed stars then migrated outward due to dynamical

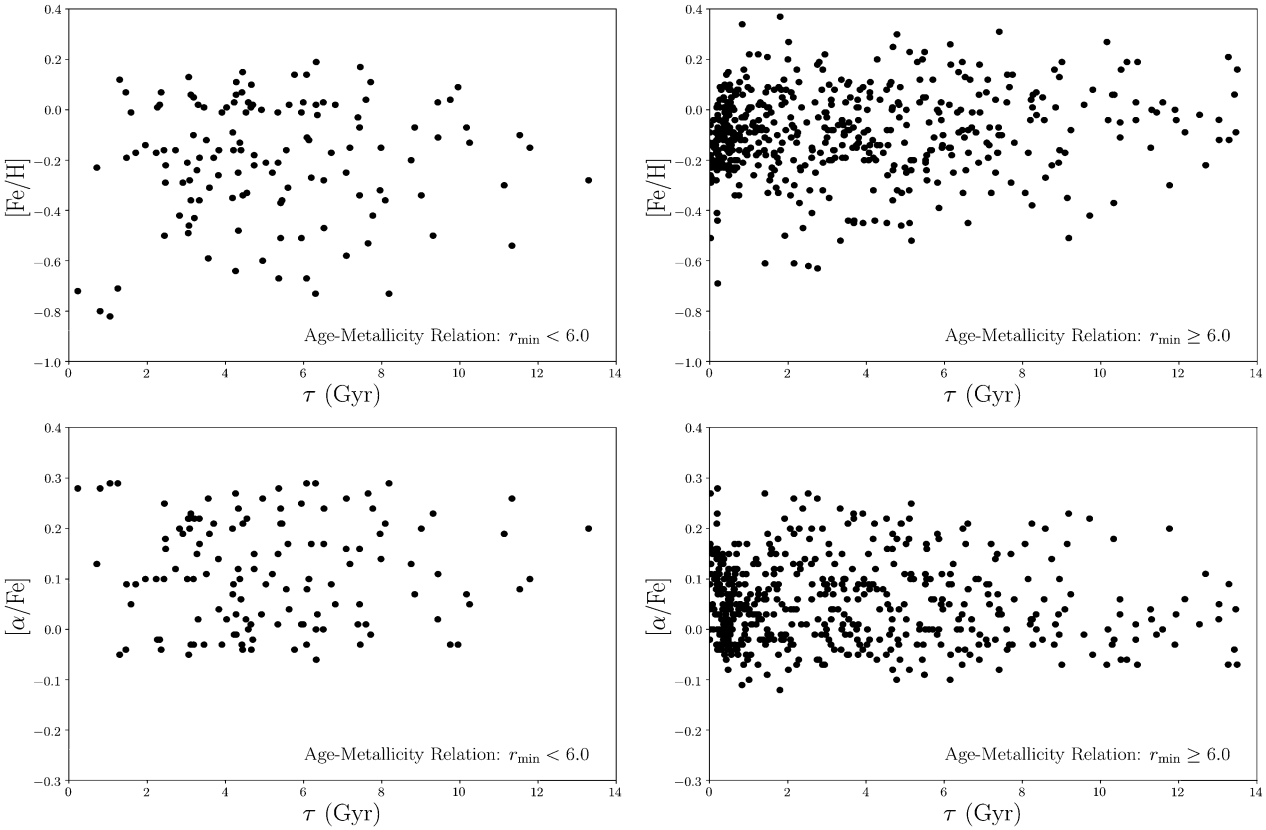

Fig. 17 Metallicity [Fe/H] and [α/Fe] against FUV-determined ages for two populations of stars sorted on the basis of perigalactic distance: $r_{min} < 6.0$ kpc (left panels) and $r_{min} \geq 6.0$ kpc (right panels). Age resolution is greater for stars younger than 6 Gyr

heating. This formation history is commonly called the "inside out" model (Matteucci and Francois 1989). In addition to the above attributes of these old stars, they also have a large range in the U velocity component towards the Galactic center, as seen in Fig. 20, which shows that stars with $r_{min} < 7.0$ kpc have a much more dispersed distribution in U than stars with $r_{min} > 7.0$ kpc. This again, is consistent with a large velocity dispersion caused by dynamical heating. Radial mixing plays its role here by redistributing stars radially over time (Loebman et al. 2011). That is, older stars are more radially dispersed, and exist at higher vertical scale heights.

Figure 19 shows the maximum vertical displacement above the Galactic plane versus perigalactic radii for the stars of which we found FUV ages. In the inside-out formation model stars with small perigalactic radii would also have larger maximum vertical displacements. Indeed many stars in this sample reflect this correlation and have a z_{max} of several kpc above the plane. However, we do note that it is not fully consistent within Fig. 19.

A high-resolution hydrodynamic simulation of a Milky Way-like galaxy, Bird et al. (2013) shows a similar scenario to what we observe here. The simulation within their work uses a fully cosmological environment and tracks age-cohorts of stars over the Galaxy's formation history. They do note that this method is less comparable to observations which utilize chemical tracers. However, it is a useful comparison for this work due to its method of tracking stars based on their ages. Bird et al. (2013) find that stars formed at redshift > 3 would have been scattered into kinematically hot configurations with thick scale heights and at shorter radial scale lengths. Younger stars are found at larger radii, but exist closer to the Galactic plane. Indeed, in this work we appear to observe the Milky Way structure following such an "inside out" pattern.

4.3 Stars with high and low [α/Fe]

In the radial migration model high-α stars which formed in the inner disk will have a steeper slope in an age-velocity dispersion relation (Schönrich and Binney 2009; Mackereth et al. 2019). It follows that a low-α population should have a flatter AVR. The Casagrande et al. (2011) sample of Geneva-Copenhagen Survey stars includes measurements of [α/Fe]. This has allowed us to split the GCS set of stars with FUV-derived ages into low-α and high-α populations using a simple cut at [α/Fe]$= 0.1$, with low-α stars falling below this threshold and high-α stars above. Admittedly this is some-

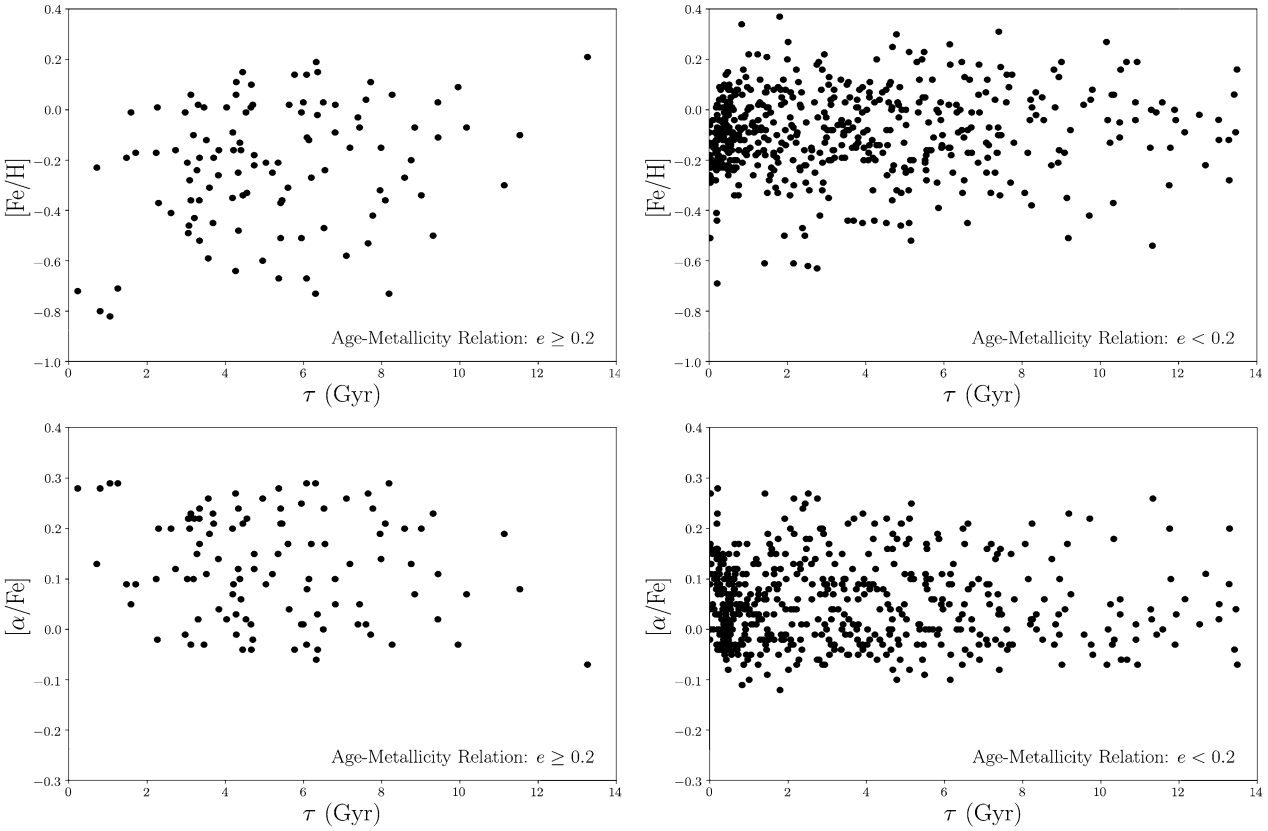

Fig. 18 Metallicity [Fe/H] and [α/Fe] against FUV-determined ages for two populations of stars sorted by orbit eccentricity: $e < 0.2$ (right panels) and $e \geq 0.2$ (left panels)

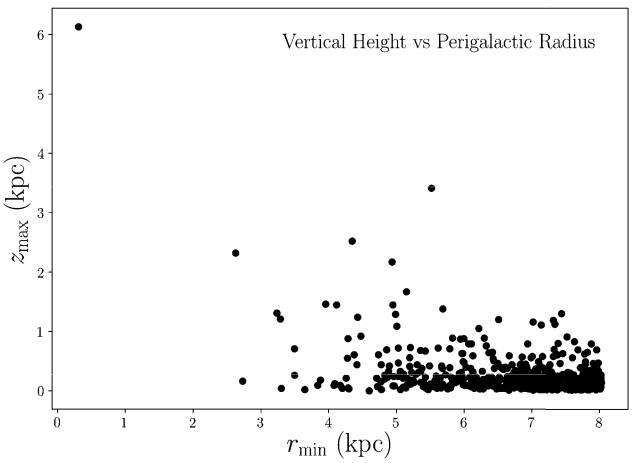

Fig. 19 Maximum vertical displacement above the Galactic plane versus perigalactic radius for the stars of which we found FUV ages

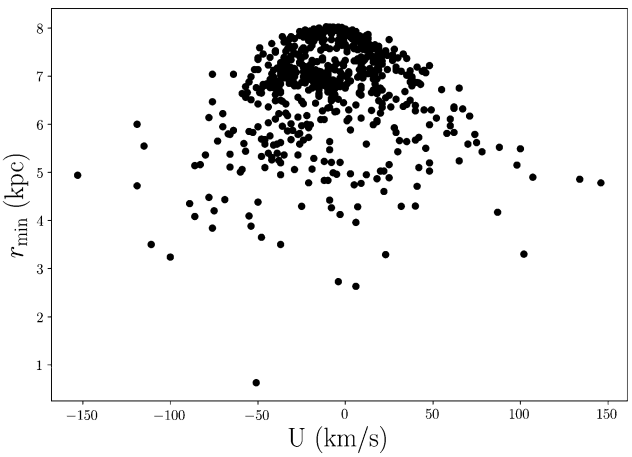

Fig. 20 Perigalactic radius versus velocity U towards the Galactic Center for the set of stars in our cross-matched sample for which FUV-ages have been determined. All values are from Casagrande et al. (2011). There is a notably greater spread in the U velocity component among stars with $r_{min} < 7.0$ kpc

thing of an arbitrary and simple distinction, and a more appropriate designation might include a Galactocentric radius consideration (see e.g., Mackereth et al. 2019). Figure 21 shows the AVR for both the low-α and high-α samples with FUV-determined ages (τ Gyr). The AVRs were fit with a power law function and have the forms

$$s = 24.58\tau^{0.31} \tag{26}$$

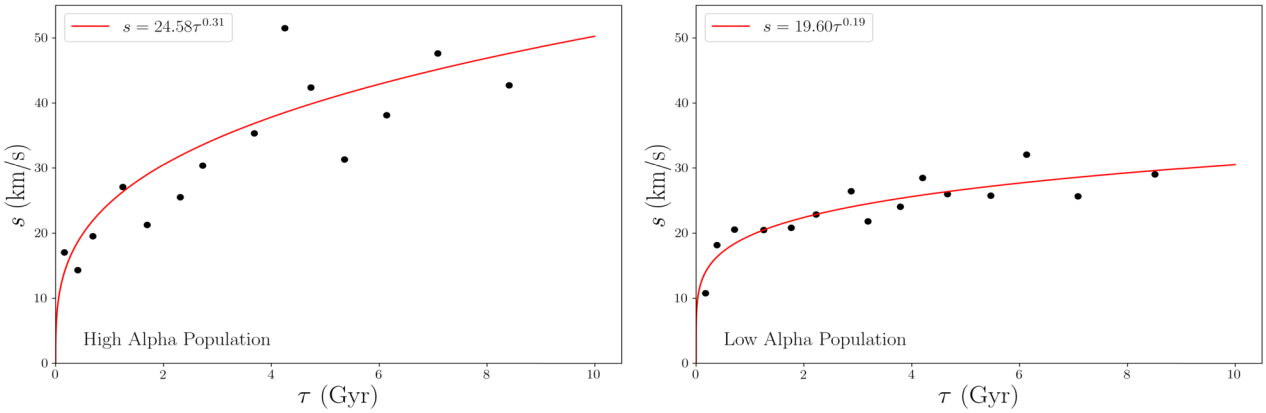

Fig. 21 AVRs constructed using FUV-determined ages for both low and high α-element samples, designated as having [α/Fe] abundance ratios less than +0.1 dex, and greater than +0.1 dex, respectively. $\tilde{\tau}$ is the median age within each bin

and

$$s = 19.60\tau^{0.19} \tag{27}$$

for the high-α and low-α populations, respectively. Here s is again the quadrature sum of the three velocity dispersions, σ_U, σ_V, and σ_W. Indeed, a flatter AVR curve is found for the lower-α population. The flatter curve indicates a younger, dynamically cooler population. This exemplifies α as a useful proxy for age when measuring the AVR.

Perhaps another instructive pair of AVRs would be constructed by parsing populations by orbit eccentricity. We did attempt to fit separate AVRs to a high-eccentricity population consisting of stars with $e \geq 0.3$ as well as a low-eccentricity population with $e < 0.3$. However, the sample with high eccentricity is a significantly smaller subsample which contributes to a quite scattered and flat AVR. The scattered nature of the plot does not allow for a well-fit power law curve, and so is not presented here.

5 Conclusion

In this work we have calibrated a relationship between *GALEX FUV* magnitude and stellar age for FGK type stars in the main sequence phase of evolution. The calibration is similar to that given in Crandall et al. (2020), however, in this case one utilizes readily available *Gaia* $(G - G_{BP})$ colors instead of Johnson $(B - V)$ colors. As such, the current calibration has the advantage of being more accessible to large numbers of stars in the *Gaia* data releases. The empirical relationship described herein allows a user to estimate the age of a Sun-like star with a *GALEX FUV* magnitude and the *Gaia* $(G - G_{BP})$ color. The calibration has the greatest age resolution for stars younger than 6-7 Gyr.

By utilizing the new FUV-age calibration, we have constructed relations between age and velocity dispersion for a set of 660 Geneva-Copenhagen Survey stars having *GALEX FUV* magnitude measurements. The AVRs have been fitted with a power law function in which velocity dispersion varies with stellar age as τ^{β}. Values found for the power-law parameter β are consistent with theoretical AVRs constructed from simulations of the orbits of Galactic disk stars that evolve by Giant Molecular Cloud (GMC) heating with $\beta \sim 0.25$. In addition, perigalactic radius and orbit eccentricity versus FUV-age plots show that our sample of stars is broadly consistent with an "inside out" model of Galactic disk formation and evolution, in which older stars are more centrally located with larger orbit eccentricities, while younger stars are found at larger radii and have smaller eccentricities.

Acknowledgements The authors gratefully acknowledge the support of the National Science Foundation of the United States through award AST-1517791. The *GALEX* photometry presented in this paper was obtained from the Mikulski Archive for Space Telescopes (MAST). STScI is operated by the Association of Universities for Research in Astronomy, Inc., under NASA contract NAS5-26555. This work has made use of data from the European Space Agency (ESA) mission *Gaia* (https://www.cosmos.esa.int/gaia), processed by the *Gaia* Data Processing and Analysis Consortium (DPAC, https://www.cosmos.esa.int/web/gaia/dpac/consortium). Funding for the DPAC has been provided by national institutions, in particular the institutions participating in the *Gaia* Multilateral Agreement.

Funding The research leading to these results received funding from the National Science Foundation of the United States under Award AST-1517791.

Declarations

Conflict of Interest The authors have no conflicts of interest to declare that are relevant to the content of this article.

References

Abadi, M.G., Navarro, J.F., Steinmetz, M., Eke, V.R.: Astrophys. J. **597**, 21 (2003)
Aumer, M., Binney, J., Schönrich, R.: Mon. Not. R. Astron. Soc. **462**, 1697 (2016)
Ballering, N.P., Rieke, G.H., Su, K.Y.L., Montiel, E.: Astrophys. J. **775**, 55 (2013)
Barbanis, B., Woltjer, L.: Astrophys. J. **150**, 461 (1967)
Bertelli, G., Girardi, L., Marigo, P., Nasi, E.: Astron. Astrophys. **484**, 815 (2008)
Bertelli, G., Nasi, E., Girardi, L., Marigo, P.: Astron. Astrophys. **508**, 355 (2009)
Bird, J.C., Kazantzidis, S., Weinberg, D.H., Duedes, J., Callegari, S., Mayer, L., Madau, P.: Astrophys. J. **773**, 43 (2013)
Bovy, J., Rix, H.-W., Hogg, D.W.: Astrophys. J. **751**, 131 (2012)
Bovy, J., Rix, H.-W., Schlafly, E.F., Nidever, D.L., Holtzman, J.A., Shetrone, M., Beers, T.C.: Astrophys. J, **823**, 30 (2016)
Brook, C.B., Kawata, D., Gibson, B.K., Freeman, K.C.: Astrophys. J. **612**, 894 (2004)
Brook, C.B., et al.: Mon. Not. R. Astron. Soc. **426**, 690 (2012)
Casagrande, L., VandenBerg, D.A.: Mon. Not. R. Astron. Soc. **479**, L102 (2018)
Casagrande, L., Shönrih, R., Asplund, M., Cassisi, S., Ramírez, I., Meléndez, J., Bensby, T., Feltzing, S.: Astron. Astrophys. **530**, A138 (2011)
Conti, A., Bianchi, L., Shiao, B.: Astrophys. Space Sci. **335**, 329 (2011)
Crandall, S., Smith, G.H., Subramonian, A., Ho, K., Cochrane, K.M.: Astron. J. **160**, 217 (2020)
Czesla, S., Schröter, S., Schneider, C.P., Huber, K.F., Pfeifer, F., Andreasen, D.T., Zechmeister, M.: (2019). https://ui.adsabs.harvard.edu/abs/2019ascl.soft06010C
Findeisen, K., Hillenbrand, L., Soderblom, D.: Astron. J. **142**, 23 (2011)
Fuhrmann, K.: Astron. Astrophys. **338**, 161 (1998)
Gaia Collaboration, et al.: Astron. Astrophys. **616**, A10 (2018)
Hänninen, J., Flynn, C.: Mon. Not. R. Astron. Soc. **337**, 731 (2002)
Haywood, M., Di Matteo, P., Lehnert, M.D., Katz, D., Gómez, A.: Astron. Astrophys. **560**, A109 (2013)
Haywood, M., Lehnert, M.D., Di Matteo, P., Snaith, O., Schultheis, M., Katz, D., Gómez, A.: Astron. Astrophys. **589**, A66 (2016)
Holmberg, J., Nordstöm, B., Andersen, J.: Astron. Astrophys. **475**, 519 (2007)
Holmberg, J., Nordström, B., Andersen, J.: Astron. Astrophys. **501**, 941 (2009)
Isaacson, H., Fischer, D.: Astrophys. J. **725**, 875 (2010)
Kim, Y.-C., Demarque, P., Yi, S.K., Alexander, D.R.: Astrophys. J. Suppl. Ser. **143**, 499 (2002)
Kokubo, E., Ida, S.: Publ. Astron. Soc. Jpn. **44**, 601 (1992)
Lacey, C.G., Ostriker, J.P.: Astron. J. **299**, 633 (1985)
Lin, J., Dotter, A., Ting, Y.S., Asplund, M.: Mon. Not. R. Astron. Soc. **477**, 2966 (2018)
Loebman, S.R., Roškar, R., Debattista, V.P., Ivezić, Z., Quinn, T.R., Wadsley, J.: Astrophys. J. **737**, 8 (2011)
Lorenzo-Oliveira, D., et al.: Astron. Astrophys. **619**, A73 (2018)
Mackereth, J.T., et al.: Mon. Not. R. Astron. Soc. **489**, 176 (2019)
Mamajek, E.E., Hillenbrand, L.A.: Astrophys. J. **687**, 1264 (2008)
Matteucci, F., Francois, P.: Mon. Not. R. Astron. Soc. **239**, 885 (1989)
Moetazedian, R., Just, A.: Mon. Not. R. Astron. Soc. **459**, 2905 (2016)
Navarro, J.F., et al.: Mon. Not. R. Astron. Soc. **476**, 3648 (2018)
Nordström, B., et al.: Astron. Astrophys. **418**, 989 (2004)
Pietrinferni, A., Cassisi, S., Salaris, M., Castelli, F.: Astrophys. J. **612**, 168 (2004a)
Pietrinferni, A., Cassisi, S., Salaris, M., Castelli, F.: Astrophys. J. **642**, 797 (2004b)
Pietrinferni, A., Cassisi, S., Salaris, M., Percival, S., Ferguson, J.W.: Astrophys. J. **697**, 275 (2009)
Prochaska, J.X., Naumov, S.O., Carney, B.W., McWilliam, A., Wolfe, A.M.: Astron. J. **120**, 2513 (2000)
Rix, H., Bovy, J.: Astron. Astrophys. Rev. **21**, 61 (2013)
Robin, A.C., Reylé, C., Fliri, J., Czekaj, M., Robert, C.P., Martins, A.M.M.: Astron. Astrophys. **569**, A13 (2014)
Roman, N.G.: Astron. J. **55**, 182 (1950a)
Roman, N.G.: Astrophys. J., **112**, 554 (1950b)
Schönrich, R., Binney, J.: Mon. Not. R. Astron. Soc. **396**, 203 (2009)
Seabroke, G.M., Gilmore, G.: Mon. Not. R. Astron. Soc. **380**, 1348 (2007)
Sierchio, J.M., Rieke, G.H., Su, K.Y.L., Gáspár, A.: Astrophys. J. **785**, 33 (2014)
Smith, G.H., Redenbaugh, A.K.: Publ. Astron. Soc. Pac. **122**, 1303 (2010)
Smith, G.H., Hargrave, M., Eckholm, E.: Publ. Astron. Soc. Aust. **34**, 49 (2017)
Soubiran, C., Bienaymé, O., Mishenina, T.V., Kovtyukh, V.V.: Astron. Astrophys. **480**, 91 (2008)
Spitzer, L., Schwarzschild, M.: Astrophys. J. **114**, 385 (1951)
Spitzer, L., Schwarzschild, M.: Astrophys. J. **118**, 106 (1953)
Strömberg, G.: Astrophys. J. **104**, 12 (1946)
Ting, Y.S., Rix, H.W.: Astrophys. J. **878**, 1 (2019)
Twarog, B.A.: Astrophys. J. Suppl. Ser. **44**, 1 (1980a)
Twarog, B.A.: Astrophys. J., **242**, 242 (1980b)
Veltx, L., et al.: Astron. Astrophys. **480**, 753 (2008)
Walker, I.R., Mihos, J.C., Hernquist, L.: Astrophys. J. **460**, 121 (1996)
Wielen, R.: Astron. Astrophys. **60**, 263 (1977)
Wright, J.T.: Astron. J. **128**, 1273 (2004)
Yi, S., Demarque, P., Kim, Y.-C., et al.: Astrophys. J. Suppl. Ser. **136**, 417 (2001)